Energy Conversion and Management: X 30 (2026) 101723

Contents lists available at ScienceDirect

Energy Conversion and Management: X

journal homepage: www.sciencedirect.com/journal/energy-conversion-and-management-x

Wave-induced losses in offshore floating PV: Physics-based modelling, sensitivity-driven quantification, surrogate-model prediction, and design-guided mitigation strategies

Sathya Shanka Vasuki [a,*], Jack Levell [b], Teddy Simanjuntak [b], Rudi Santbergen [a], Olindo Isabella [a]

[a] Photovoltaic Materials and Devices, Delft University of Technology, Mekelweg 4, Delft, 2628 CD, South Holland, The Netherlands
[b] Shell Global Solutions International B.V., Grasweg 31, 1031, Amsterdam, The Netherlands

ARTICLE INFO

Keywords:
Offshore floating solar
Wave induced losses
Hydrodynamic analysis
Energy yield analysis
Sensitivity analysis
Surrogate modelling

ABSTRACT

Offshore floating photovoltaics (OFPVs) emerge as a promising solution to overcome land constraints associated with inland renewable energy deployment. However, as OFPVs are still a developing technology, several performance-related uncertainties persist. The reduction in energy yield caused by wave-induced losses (WIL) is one such critical uncertainty that needs to be understood, quantified and minimised. To address this need, this work introduces a physics-based modelling framework that couples validated hydrodynamic simulations with opto-electrical analysis to accurately estimate WIL. An extensive sensitivity analysis is then carried out, performing over 100 simulations by systematically varying both design and environmental parameters. The results show that WIL ranges between 1%–30% on an hourly basis and exhibits a nonlinear dependence on both parameter groups. The resulting dataset is then used to develop **SWIFT** 1.0 - a surrogate model capable of predicting WIL across a wide range of design and operating conditions, achieving an average absolute RMSE of 3% relative to the physics-based model. The insights from **SWIFT** 1.0 are finally used to provide practical measures that minimise WIL at a system design level. Overall, this work provides a complete pathway to model, quantify, predict, and minimise WIL, promoting confident and scalable OFPV deployment.

1. Introduction

COP28 held in 2023, had proposed a target to member countries aimed at achieving a global renewable energy capacity of ~11 TW by 2030 [1–5]. With solar energy being one of the key drivers in energy transition, achieving this target would require a 9 time increase in the installed capacity compared to the installations in 2024 (~2.1 TW) in the span of 5 years [1–4]. With growing population and increasing competition from agricultural conservation, industrial development, and socio-environmental constraints, there is a significant uncertainty in the availability of land for renewable energy installations — both now and in the future—highlighting the critical spatial bottleneck that might affect the pace of the energy transition [6]. Therefore, innovative technologies that can mitigate this uncertainty is both timely and necessary. This is where new technologies such as offshore floating photovoltaics (OFPV) could be a promising and reliable solution [6–12].

However, as with any emerging technology, OFPVs face several technological challenges — one of the most critical being the prediction of the Energy Yield (EY). Understanding the long-term EY of OFPV systems is not only essential for technology development and design optimisation, but also for large-scale deployment. Yet, our ability to confidently quantify it remains limited, as most existing installations are recent (within the last 2–3 years) making long-term performance prediction all the more difficult. Unlike Ground mounted PV, EY prediction for OFPVs is complicated due to several offshore-specific factors such as dynamic motion (effect of waves), cooling (effect of water temperature), optical changes (effect of shading and soiling), and long-term degradation (effect of salinity and mechanical loads) [6]. These effects are highly site- and design-dependent, making accurate prediction essential yet extremely challenging.

Among all influencing factors, the dynamic motion caused by waves, wind, and currents is particularly unique to OFPVs and has a significant impact on the EY, as it continuously alters the module orientation (tilt, θ_t and azimuth, a_z) over time. For instance, in unit archetypes (a unit archetype is defined as a single geometrical unit of the floater design on which the PV modules are mounted) that can host multiple PV modules on a single floater, all modules on one floater share the

* Corresponding author.
E-mail address: S.S.ShankaVasuki@tudelft.nl (S.S. Vasuki).

https://doi.org/10.1016/j.ecmx.2026.101723
Received 13 January 2026; Received in revised form 23 February 2026; Accepted 2 March 2026
Available online 3 March 2026

Abbreviations

COP28	28th UN Climate Change conference
EY	Energy yield
LEP	Large elevated platforms
LRP	Large rigid pontoons
OFPV	Offshore floating photovoltaics
RP	Rigid pontoon
WIL	Wave induced losses
α	Random phase [deg]
β	Discrete wave direction [deg]
χ/θ_w	Wave angle to global x-axis [deg]
γ	Peakedness Parameter [–]
μ	Standard deviation
ω	Wave frequency [rad/s]
σ	Mean
θ_t	Tilt angle [deg]
$A_{z,\,sun}$	Solar Azimuth [deg]
A_z	Azimuth angle [deg]
$C_{x/y/z}$	Rotational damping [N m/(rad/s)]
D_f	Diameter of LEP columns [m]
$Draft$	Submerged distance [m]
h_{sun}	Solar Altitude [m]
H_f	Height of LEP columns [m]
H_s	Significant wave height [m]
I_{mpp}	Max power point current [A]
$I_{(xx/yy/zz)}$	Moment of inertia [kg m^2]
k	Wave number [m]
k_{moor}	Mooring line stiffness [N/m]
$K_{(xx/yy/zz)}$	Radii of gyration [m]
L_{moor}	Length of mooring lines [m]
L_f	Length of the floaters/deck [m]
$M_{floater}$	Mass of individual unit [kg]
m_{farm}	Mass of the entire farm [kg]
N_{PV}	Number of PV modules per floater [–]
N_d	Number of wave directions
N_f	Total number of floaters in the farm
N_{conn}	Total number of connectors [–]
N_{moor}	Total number of mooring lines [–]
N_m	Number of wave frequencies
PT_{moor}	Pretension in mooring lines [N]
R^2	Coefficient of determination
$R_{(x/y/z)}$	Rotational stiffness [Nm/rad]
t	Time [s]
T_f	Thickness of the floaters/deck [m]
T_p	Peak wave period [s]
V_{mpp}	Max power point voltage [V]
W_f	Width of the floaters [m]
X_{QCorr}	Quantile corrected response [deg]
X_{RAO}	Time series response of DoFs [deg]
X_{vCorr}	Global variance corrected response [deg]
$x_g,\ y_g$	CoG coordinate of each floater [m]
DHI	Diffuse horizontal irradiance [W/m^2]
DNI	Direct normal irradiance [W/m^2]
Gap	Gaps between adjacent floaters [m]
GHI	Global horizontal irradiance [W/m^2]
SEI	Spectral energy index [–]

same instantaneous orientation, resulting in stochastic cycles of time-varying plane-of-array irradiance differences, as shown in Fig. 1(a). Similarly, in unit archetypes where each floater accommodates only one PV module, each module moves independently, causing stochastic plane of array irradiance fluctuations across individual modules at every instant, as illustrated in Fig. 1(b).

In both cases, there are conditions where a PV module (or a group of modules) alternately faces towards and away from the sun, thereby leading to a gain or loss in EY relative to a reference (initial) orientation. This effect is termed as wave-induced plane of array irradiance variation. When all PV modules in such systems are connected in series to form a modular farm, these non-uniform plane of array irradiance conditions create differences in the current generated by each module (or group of modules). Since the overall string current is limited by the lowest-performing module (or set of modules), this leads to additional EY losses known as wave-induced mismatch losses. The combined effect of these two phenomena constitutes to the total wave-induced losses (WIL) [13]. Therefore, understanding WIL in detail forms the central scope of this work.

2. Literature review, research gaps and contribution of this work

Literature synthesis: The estimation of WIL requires two types of analysis: hydrodynamic analysis (to estimate floater motion) and EY analysis (to translate motion into power output). As different studies use different approaches to understand this effect, a structured comparison is needed to understand what has been done so far. Table 1 therefore summarises key WIL studies based on: the method used (experimental or computational), the system archetype and farm configuration examined, the hydrodynamic modelling approach (whether

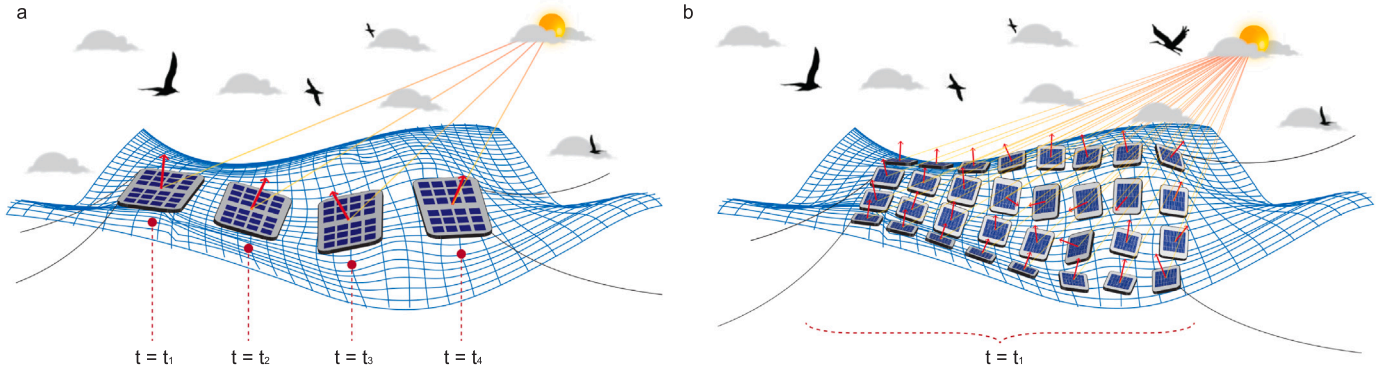

Fig. 1. Effect of dynamic motion — concept of wave-induced losses. (a) For archetypes that host multiple PV modules on a single floater, all modules on that floater share the same instantaneous orientation, resulting in stochastic cycles of time-varying plane-of-array irradiance differences. (b) For archetypes where each floater accommodates only one PV module, each module moves independently, leading to stochastic plane-of-array irradiance fluctuations across individual modules at every instant. Note: the blue mesh represents the waves and the red arrows represent the normal vector of the PV module.

Table 1
Literature Review of relevant studies focusing on modelling, evaluating and quantifying wave induced losses.

Ref.	Year	Method	Archetype[b]	Config.	Hydrodynamic analysis				EY	Tool	Val.[a]	SA[a]	WIL (%)
					Type[a]	M-C[a]	Geo-location	Waves					
[14]	2019	Sim.	RP[c]	String	Not reported	Not reported	Oosterschelde, North Sea	Not reported	✓	Inhouse, PVLIB	×	String length h/λ ratios	3-9
[15]	2020	Sim.	RP	Single	2D	✓	North Sea	JONSWAP	✓	Matlab, Simulink, PVLIB	×	×	+13[d]
[16]	2021	Both	RP	Not reported	3D	Not reported	Marsaxlokk	Not reported	Irradiance	Microsoft Excel	✓	Pitch, roll, yaw	0.38–2.52[e]
[17]	2022	Sim.	RP/LRP	Array	Not reported	Not reported	Not reported	Not reported	✓	Matlab, Helioscope	×	Interconnection schemes Shading patterns	27-56[f]
[18]	2023	Sim.	RP	Array	3D	✓	Sishiliwan Bay	Fifth order Stokes	✓	Ansys AQWA, OrcaFlex, Simulink	×	Wave Steepness	6.5–15
[19]	2023	Sim.	LRP	Single	2D	✓	East coast of China, West coast of India	Regular	✓	Matlab, Simulink	~	Wave height, wave period, Wind speed, Pretilt angle	0.2–3.4
[20]	2023	Both	BUY	Single	3D	Not reported	Chinese sea	Regular	Irradiance	Ansys AQWA, Inhouse	✓	Sea states Pretilt angle	2–5[g]
[21]	2023	Sim.	LRP	Single	2D/3D	Not reported	Pagasitikos Gulf SE Evia Island	JONSWAP	✓	Inhouse	✓	Location, h, T_p, ψ	8–9[h]
[22]	2024	Sim.	LRP	Single	2D	Not reported	North Sea	JONSWAP	✓	Inhouse	~	Geometry	0.1–14.6
[23]	2024	Sim.	LRP	String	2D	Not reported	North Sea	JONSWAP	✓	Inhouse, PVlib	×	Geometry String length Floater material	0.1–30
[24]	2024	Exp.	VPOT	Single	3D	✓	Not relevant	Regular	✓	Not relevant	Not relevant	Wave amplitude Frequency	1.5–12.7
[25]	2025	Sim.	RP	String	Not reported	Not reported	2 locations: near equator, higher latitude	Pierson-Moskowitz	✓	3DFloat, PVmismatch	Irradiance Validated	$H_s, T_p, \psi, \theta_{pre}$ String length	3.3–6.7
[26]	2025	Sim.	LEP	Array	3D	✓	Fujian province	JONSWAP	✓	OrcaFlex, Inhouse	✓	Sun path, Pretilt angle	1–25
[27]	2025	Both	HPIT	String	3D	✓	Not reported	Regular	✓	Inhouse	✓	Wave height, wave period, Number of modules, Pretilt angle	~12
[28]	2026	Both	LEP	Array	3D	✓	Not reported	JONSWAP	✓	Matlab	✓	Wave height, wave period, Wave direction, connector type	2.5%
[29]	2026	Sim.	LRP	Single	3D	✓	Mediterranean Sea	JONSWAP	✓	Matlab	✓	Pretilt angles	0.05–1.1
[30]	2026	Both	Flexible	String	3D	✓	Not reported	Regular	✓	Inhouse	✓	Plate thickness, connector length, Module number	+5
[31]	2026	Both	Catamaran	Single	3D	✓	Not reported	Regular	✓	Matlab based digital twin model	✓	Light incidence angle, Wave amplitude, wave length	Not explicitly reported
This work	–	Sim.	RP, LRP, LEP	String, Array	3D	✓	North Sea, Great Australian Bight	ERA5 derived	✓	Ansys AQWA PVMDToolbox	✓	Multiple parameters varied	See Section 4.3

[a] Type indicates whether the hydrodynamic simulations were performed in 2D or 3D; M–C indicates whether interconnections between floaters and the mooring lines were included in the study; Val indicates whether the reference study reported validation of their model; and SA indicates whether a sensitivity analysis was conducted and specifies which parameters were varied.

[b] RP — Rigid pontoon, LRP — Large rigid pontoon, LEP — Large elevated platform, BUY — Bouy floaters, VPOT — Vertical pontoon truss, HPIT — Horizontal pipe truss. The archetype nomenclature are inspired from the classification made in [6].

[c] Since the article mentions single-module High-Density Polyethylene floaters, an RP archetype is assumed.

[d] This is the relative difference between output energy from two systems on land and at sea.

[e] This represents the mismatch in insolation due to pitch, roll and yaw movements.

[f] This is the relative difference between power output of the system with uniform and partial shading.

[g] This is the difference in the irradiance received by the PV modules.

[h] This is the relative difference between output energy from systems on inland and at sea.

2D or 3D simulations were performed, whether mooring lines and interconnectors were included, the geolocation considered, and the wave conditions applied), and whether EY was evaluated. The table also indicates whether a sensitivity analysis was conducted (including the parameters that were varied) which is critical for understanding what factors (design or environmental) govern WIL. Finally, the reported WIL ranges are summarised. We use this structured overview to identify where the literature is strong, where it is inconsistent, and what is missing across the hydrodynamic, EY, and sensitivity-analysis parts of the WIL estimation chain. These observations define the critical research gaps discussed next.

Research Gaps: Table 1 shows that existing literature has made substantial progress in recent years, specifically in the modelling domain, to understand the concept of WIL. The magnitude of reported WIL values also clearly demonstrate that WIL is an important phenomenon that cannot be neglected in EY predictions of OFPV systems. However, the same reported WIL values also indicate a wide and inconsistent spread (0.1% to 56%), which leads us to identify four critical research gaps.

(1) Modelling inconsistencies: While foundational modelling techniques have been proposed in studies such as [15,16,19,21–23,25,26,29], a complete modelling framework capable of resolving the full hydro–opto–electrical coupling still remains missing. This is largely due to the inherent complexity of modelling this problem, where studies opt to make certain assumptions and simplifications to make the process viable. For instance, on the hydrodynamic side, some models are restricted to 2D sectional analysis or limit the floating structure's motion to only one or two axes, such as pitch or roll, which fails to capture the full stochastic motion (roll, pitch, and yaw) of an OFPV system in offshore conditions [15,19,21]. Additionally, some frameworks use simple sinusoidal wave inputs that do not represent the irregular nature of actual offshore waves, while others assume that the floater simply follows the wave, ignoring the wave–structure interaction [16,22,25]. Some studies also use linear approximations in resolving the wave–structure interaction that do not include non-linear effects in multi-interconnected systems [29]. On the electrical side, some studies use linear power-conversion formulas or rely on commercial PV modelling tools typically designed for ground-mounted systems. These

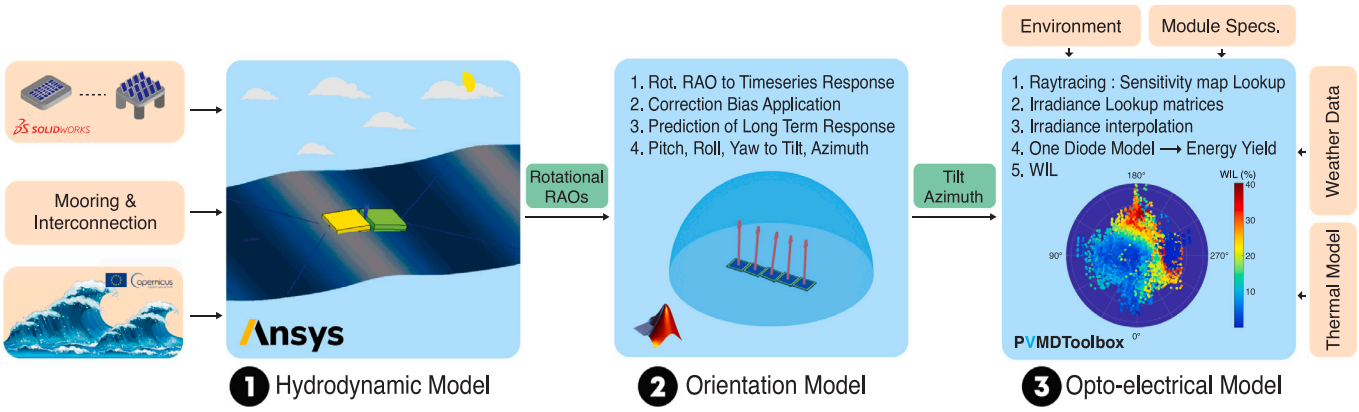

Fig. 2. Overview of the numerical modelling framework used in this work, beginning with (a) the hydrodynamic modelling, where the fluid–structure interaction is solved and the resulting motion time series are obtained and used as input to (b) the orientation modelling, in which the hydrodynamic response is converted into time-series tilt and azimuth angles. These orientation time series then serve as input to (c) the opto-electrical modelling, where the corresponding WIL is computed.

tools do not specifically incorporate OFPV effects and may therefore not provide the actual realistic performance of an OFPV system. While some studies attempt to calculate the dynamic plane-of-array irradiance to quantify the WIL, they often make varying simplifications in this regard [16,17,26,29]. These combined simplifications in both modelling areas ultimately lead to inconsistent in reported WIL.

(2) Incomplete quantification: The second gap relates to how effectively WIL is quantified in terms of its dependence on design and environmental parameters. While a few recent studies have used sensitivity analysis as a means to quantify WIL, the parameters they vary are often limited. For instance, the majority of research focuses on varying wave properties, as shown in Table 1 [14,16,18,20,21,24,25], while only a few studies vary design-based parameters [17,22,23,25,27,28,30]. Consequently, the majority of studies varying wave properties typically do not vary geometrical properties, and vice versa. Furthermore, most research focuses on only one type of archetype design with either single floaters or string-connected systems [15,20–25,27,29–31], with only a few examining array-level systems [17,18,28]. Because of this partial quantification, only limited insights can be drawn into how design and environmental factors govern WIL, thereby leading to highly scattered WIL values (see Table 1). Hence, a systematic sensitivity analysis that quantifies WIL by varying both design-based factors (such as unit archetype and farm-level properties) alongside environmental factors (such as wave and solar properties) for both string- and array-level systems is missing.

(3) Lack of data-driven models: The third gap relates to the disconnect between physics-based models and long-term WIL projections. Currently, the field is constrained by an inherent accuracy–duration trade-off. While studies either propose physics-based models or perform experiments to estimate WIL, the sheer complexity of the problem limits their scope. As a result, some studies are restricted to reporting only short-term projections, spanning from minutes to days [19,20,24,26–28,30,31]. However, short-duration reporting does not necessarily indicate high model complexity, as some simplified frameworks are also applied at these scales. In contrast, studies reporting long-term projections, such as monthly or annual values, may still employ physics-based formulations but often rely on modelling simplifications or temporal data averages [15–17,21–23,25,29] to report performance metrics. This is not surprising, as performing long-term experiments is not practically feasible, and the numerical evaluation of physics-based models for such temporally resolved, multi-scale problems requires prohibitively high computational effort. This gap is therefore not due to a lack of research effort but is an inherent computational limitation within the field. Recent studies such as [31] have begun exploring data-driven modelling approaches as alternatives, but these remain quite rudimentary in their current state. As a result, a robust data-driven model that can bridge this computational bottleneck is still largely missing.

(4) Lack of design guidance: The fourth gap pertains to the difficulty of deriving actionable recommendations to minimise WIL at the system design level. Because of the limitations mentioned above, such recommendations are currently challenging to develop and are largely missing from the literature.

Objective: To address these four critical research gaps, this work formulates four corresponding research questions: **RQ1.** How to develop a physics-based integrated modelling framework that accurately couples 3-D wave-structure hydrodynamics with opto-electrical performance? **RQ2.** How to comprehensively quantify WIL through a multi-parameter (geometrical + environmental) sensitivity analysis across diverse OFPV archetypes? **RQ3.** How to formulate a computationally efficient, data-driven surrogate model to predict long-term WIL for different designs and operating conditions? **RQ4.** How to derive actionable, configuration-based design recommendations to minimise WIL in OFPV systems?

Novelty and Scientific contribution: As shown in Table 1, the majority of studies address the WIL estimation chain in parts rather than as a single, end-to-end problem. Hydro–opto–electrical modelling, sensitivity-based quantification, and long-term prediction are typically treated separately, which contributes to the wide and inconsistent spread in reported WIL values and hinders confident global-scale deployment decisions. The novelty of this work is that it integrates all these elements into one consistent workflow, enabling WIL to be modelled, quantified, and predicted across diverse designs and conditions, thereby providing design-actionable insights. The scientific contributions of this work are: **(1) End-to-end physics-based modelling framework:** We provide a complete modelling framework that couples 3-D multibody wave–structure hydrodynamics with orientation-resolved opto-electrical modelling, applicable to different designs and operating conditions. This directly addresses the modelling inconsistencies identified in the literature. **(2) Systematic multi-parameter quantification:** We perform a comprehensive sensitivity analysis in which design-, connector-, mooring-, and environment-based parameters are jointly varied to comprehensively characterise how WIL depends on both design and environmental factors across diverse OFPV archetypes. **(3) Computationally efficient data-driven surrogate model:** We develop and propose a surrogate model which, to the authors' knowledge, is a first-of-its-kind for OFPV WIL prediction. This enables long-term, temporally resolved WIL forecasting across a wide range of configurations without relying on computationally expensive physics-based simulations, enabling the realisation of global-scale WIL projections. **(4)**

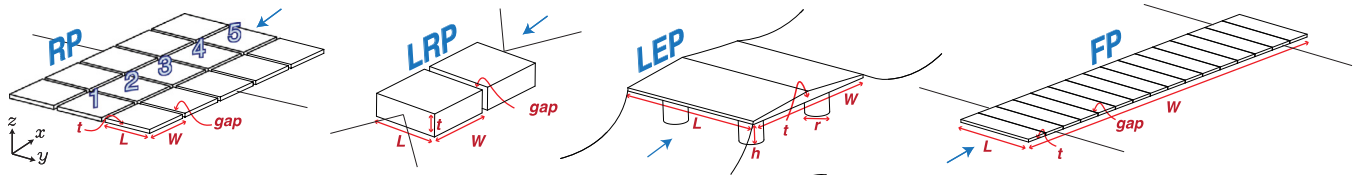

Parameter	RP	LRP	LEP	FP
1. Geometrical properties				
Length (m)	1.88	45	10	300 (18.35)
Breadth (m)	1.88	45	10	60
Thickness (m)	0.14	15	0.2+0.437	2
Radius (m)	-	-	0.75	-
Height (m)	-	-	2	-
Draft (m)	0.1	9	0.91	0.5
Gap (m)	0.15	5	1	0.4
2. Mass and inertial properties				
Mass (ton)	0.346	18291.9	6.601	9225
CoG (m)	0.1	8.72^{+}	1.76	1*
K_{xx} (m)	0.48	16.8	3.1	17.33*
K_{yy} (m)	0.48	16.8	3.06	5.44*
K_{zz} (m)	0.62	18.375	4.22	18.15*

Parameter		RP	LRP	LEP	FP
3. Wave properties					
Wave theory		JONSWAP	Regular	Regular	Regular
Amplitude or H_s (m)		1.01	-	1.76	1
ω (rad/s)		1.525	0.415-1.04	-	0.415-1.014
Gamma (γ)		4	-	-	-
Direction (deg)		180	180	0	0
Water depth (m)		36	35	18	58.5
4. Mooring line properties					
Type		Linear	Linear	Catenary	Linear
Unstretched length (m)		12.95	161	58.556	161
Stiffness (kN/m)		2.01	64.19	⊗	64.19
Pretension (kN)		1.71	2337.4	⊗	2337.4
Diameter (mm)		-	-	35	-
Submerged weight (N/m)		-	-	229.07	-
Maximum Tension $^{\oplus}$(kN)		-	-	1125.48	-
Axial Stiffness (MN)		-	-	123.72	-
5. Connector properties					
Type		Ball socket	Hinge	Hinge	Hinge
Stiffness (Nm/rad)	R_x	1.7	$5.73 \times 10^{10*}$	5.73×10^{6}	2.64×10^{10}
	R_y	1.4	-	-	-
	R_z	84	-	-	-
Damping ($Nm/(rad/s)$)		0	0	5.73×10^{6}	-

$^{+}$ Measured from the keel.
* These parameters are either derived through calculations or determined through trial testing, as they are not explicitly reported in the reference study.
$^{\oplus}$ Tension capacity limit of the mooring line segment.
$^{\otimes}$ These parameters are internally calculated within AQWA and are not user inputs. Hence, these fields are left blank.

Fig. 3. Design, geometric, mass, inertial, wave, connector, and mooring-line input properties for the validation cases. Note: All parameters shown in the figure correspond to the conditions used in the reference article, unless explicitly stated otherwise in the main text.

Actionable design recommendations: Based on the sensitivity analysis and surrogate results, we provide a practical set of configuration-based design guidelines to minimise WIL, offering system designers concrete recommendations to optimise their designs.

Collectively, these contributions reduce the overall uncertainty surrounding WIL and provides a complete, physics-informed understanding of this phenomenon.

3. Numerical modelling framework and validation

We begin this work by first providing a detailed overview of the modelling framework, aimed at addressing **RQ1** on *How to develop a physics-based integrated modelling framework that accurately couples 3-D wave-structure hydrodynamics with opto-electrical performance?* In this study, a three-step approach is adopted to model WIL, as illustrated in Fig. 2. The steps are as follows: (1) *Hydrodynamic modelling:* first, the wave–structure interaction is simulated to obtain the six degrees of freedom (DoF) response (surge, sway, heave, roll, pitch, yaw) of the OFPV system under a given wave condition. (2) *Orientation modelling:* next, the resulting system response is translated into solar orientation parameters (θ_t and A_z) suitable for use in the opto-electrical modelling. (3) *Opto-electrical modelling:* finally, the time-varying module orientations are used to compute the dynamic plane of array irradiance, which is then used to estimate the system's electrical performance by quantifying the EY to thereby calculate the WIL. The following sections provide a detailed explanation of each modelling step, including validations where appropriate.

3.1. Hydrodynamic modelling

The first step in modelling WIL is to compute the dynamic motion response of the OFPV system when subjected to environmental loads (see Fig. 2). To achieve this, a hydrodynamic analysis is required to characterise the wave–structure interaction. In this work, *ANSYS AQWA* is used for this purpose [32] (the rationale behind selecting *AQWA* is discussed in detail in Section S2 in the supporting information). The hydrodynamic analysis is based on potential-flow theory, which assumes the fluid is inviscid, incompressible, and irrotational. The solver solves the Laplace equation subject to linearised free-surface and impermeable seabed boundary conditions, with a radiation condition imposed at the far field to ensure scattered waves decay at infinity [32]. To ensure the reliability and versatility of this hydrodynamic tool for OFPV applications, validating the model is extremely crucial. Hence, in this work, a detailed validation study is performed across four different archetypes—rigid pontoon (RP), large rigid platform (LRP), flexible pontoon (FP) and large elevated platform (LEP) —which represent some of the most commonly adopted practical OFPV designs (more about these archetypes will be discussed in the upcoming sections). Therefore, the objective of this validation is twofold: to verify the accuracy and applicability of the hydrodynamic model using AQWA for OFPV applications, and to provide a concrete, benchmark reference model for different archetypes that can be used by the research community for future OFPV simulations.

The validation procedure for all archetypes follows a few general steps, beginning with the definition of a set of input parameters—such as the geometrical dimensions, mass and inertial properties, external environmental factors, mooring line parameters, and inter-floater connector

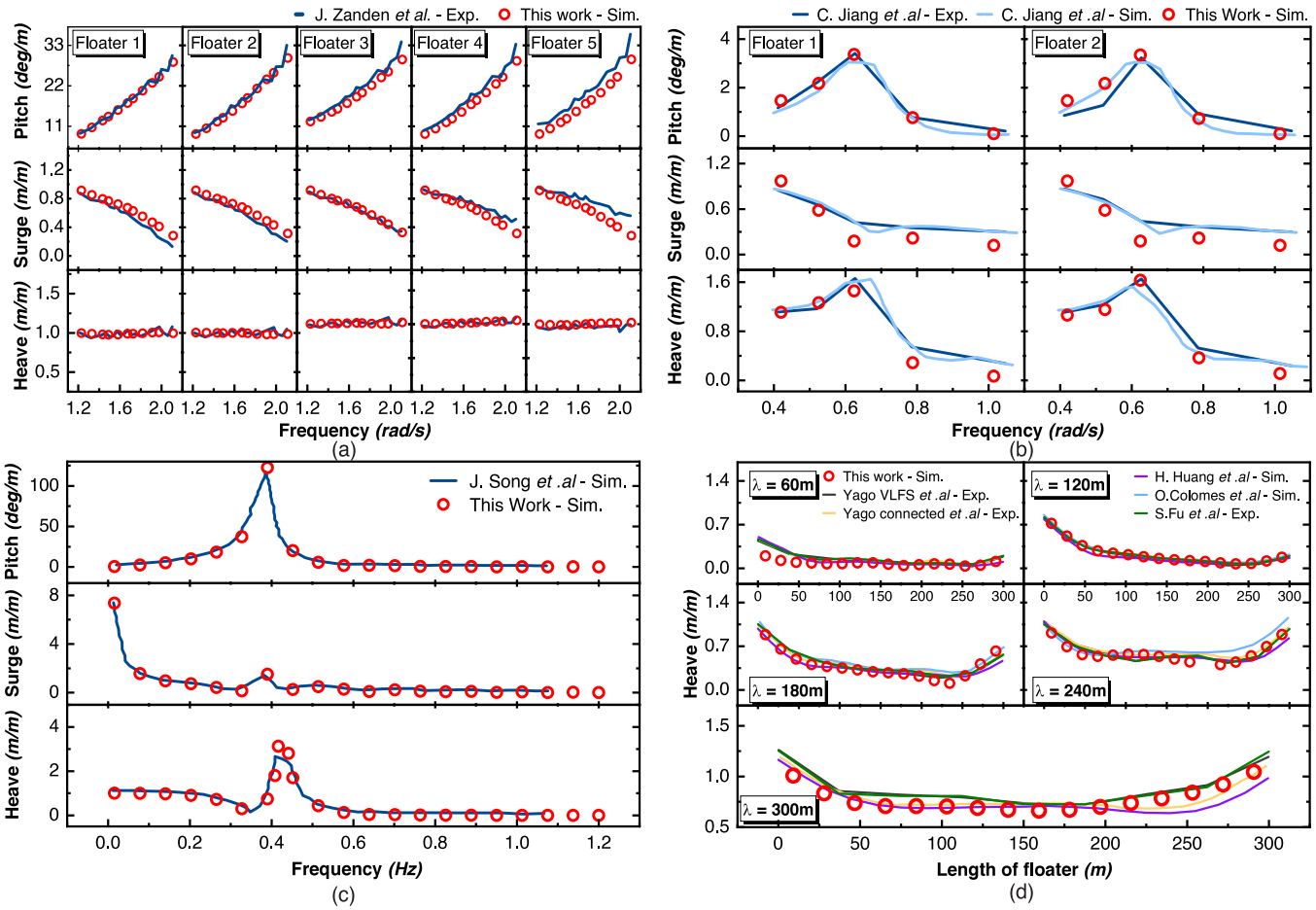

Fig. 4. Hydrodynamic validation results of each archetype as displayed in Fig. 3: (a) rigid pontoon (RP) archetype, (b) large rigid pontoon (LRP) archetype, (c) large elevated platform (LEP) archetype, and (d) flexible pontoon (FP) archetype. Note: (a–c) are the RAOs for individual floaters as mentioned in the respective plot and in (d) each point represents the heave response at the centre of gravity of each floater.

properties—which are either derived from or directly extracted from the reference studies (the detailed values of the input parameters used for each validation study are summarised in Fig. 3). In particular, the mass corresponds to the total mass of the system, while the inertial properties are characterised by the radii of gyration (K_{xx}, K_{yy}, K_{zz}) of each unit floater about its centre of gravity. The resulting simulation outputs, i.e., the Response Amplitude Operators, RAOs (see Section S1 in the Supporting Information for the definition.) in this case, are then compared against the corresponding reference studies through selected degrees of freedom as reported in the respective reference study. By following the above steps, a complete hydrodynamic simulation can be performed in *ANSYS AQWA* whose outputs are the input to next modelling step as highlighted in Fig. 2. The results of each validation study are discussed in detail below.

- **Rigid Pontoon (RP):** The hydrodynamic model for the RP archetype was validated against a reference wave tank experiment [33,34] involving a modular FPV system consisting of 15 interconnected floaters, where each floater hosted a single PV module along with certain marine growth (accumulation of biological material that makes the floater heavier than usual) as reported in [33,34]. The geometrical properties of the system were extracted from the reference study, as shown in Fig. 3, and modelled accordingly in *ANSYS AQWA*. For the connections between adjacent floaters, a total of 44 ball-and-socket joints (a ball-and-socket joint permits rotation about all three axes while constraining translational motion) were used, with the stiffness about each rotational axis extracted from the reference article, as also indicated in Fig. 3. The array was moored to the basin sidewalls using two linear mooring lines, replicating the experimental configuration. The hydrodynamic simulation was performed under irregular, long-crested wave conditions using a JONSWAP wave spectrum. This spectrum was constructed using the spectral information (H_s, ω, γ) provided in the reference studies [33,34] (see Fig. 3). The wave heading was set to 180°, directed towards the origin from the x-axis, as illustrated in Fig. 3. Using these inputs, both Hydrodynamic diffraction (frequency domain) and hydrodynamic response (time domain) analyses were conducted (more details in Section S2 of the supporting information), and the pitch, surge, and heave RAOs were extracted from the frequency statistical analysis (more details in Section S2 of the supporting information) for five representative central floaters (see Fig. 3) and compared with the experimental data, as shown in Fig. 4(a). From this comparison, it can be seen that the simulated results from AQWA show strong agreement with the experiments, with RMSE values ranging between 1.1–3.8 deg/m for pitch, 0.02–0.15 m/m for surge, and 0.02–0.04 m/m for heave. Additionally, although the pitch RAO in the plot appears to increase indefinitely, this is not the case. The pitch response decreases at higher wave frequencies (beyond 4 rad/s), but these frequencies were excluded from the plot to match the frequency range reported in the reference study. The full pitch RAO profile, including the higher-frequency decay, is provided in Section 2 of the supporting information. Overall, this validation confirms that the coupled hydrodynamic model accurately captures the multi-body interaction and dynamic response of the modular RP array using *ANSYS AQWA*.
- **Large Rigid Pontoon (LRP):** In this case, both a wave tank experiment and a numerical simulation were used as references to

validate a modular large rigid platform-type archetype consisting of two floaters, as shown in Fig. 3. Although the reference study primarily focused on analysing the hydrodynamics of articulated floating structures serving as building blocks for artificial islands [35,36], this configuration can be considered a good representative of an LRP-type archetype, where each floater can support multiple PV modules (even though the scale of a floating island is much larger than that of a typical unit LRP archetype). In this study, a full-scale system was modelled, where the two floaters were connected using a single hinge connector (a hinge connector allows rotation only about one axis and restricts translational motion). The entire system was moored to the basin sidewalls using four linear mooring lines, replicating the reference configuration. To validate the model, a frequency statistical analysis was performed in *ANSYS AQWA*. Because this approach requires an irregular wave spectrum as an input, the experimental regular waves (five frequencies ranging from 0.415 to 1.04 rad/s) were represented using an equivalent theoretical JONSWAP spectrum. To ensure numerical equivalence with the frequencies used in the experimental study, the peak frequency (ω_p) was set to 0.48 rad/s, the significant wave height (H_s) to 1 m, and a peak enhancement factor of $\gamma = 3.3$ was used. This specific spectral configuration ensured that sufficient energy density was maintained across all frequencies of interest, providing a high signal-to-noise ratio for stable RAO extraction, even at the spectral tails. The pitch, surge, and heave RAOs for both floaters were then extracted at the same discrete frequencies corresponding to each experimental and numerical reference data, as shown in Fig. 4(b). From the plot, it can be seen that the simulated results show strong agreement with the reference study, with RMSE values ranging between 0.13–0.46 deg/m for pitch, 0.17–0.18 m/m for surge, and 0.11–0.18 m/m for heave confirming the accuracy and reliability of the hydrodynamic model for the LRP archetype.

- **Large Elevated Platform (LEP):** In this case, a numerical simulation was used as the reference to validate a large elevated platform-type archetype consisting of a single floater [37]. No connectors were used in this setup, as only a unit archetype was modelled, and the system was moored to the seabed using non-linear catenary mooring lines, as shown in Fig. 3. Unlike the previous three archetypes, only the hydrodynamic diffraction analysis (more details in Section S2 of the supporting information) was performed in this case to validate the RAOs against the reference study. The pitch, surge, and heave RAOs for the floater were extracted and are shown in Fig. 4(c)[1]. As seen in the plot, the simulation results show good agreement with the numerical reference data, with RMSE values of 4 deg/m for pitch, 0.25 m/m for surge, and 0.2 m/m for heave—confirming the reliability of the hydrodynamic model for this archetype.
- **Flexible Pontoon (FP):** In this case, multiple reference studies employing both wave tank experiments and numerical simulations were used to validate a flexible pontoon-type (FP) archetype [38–41]. The reference works primarily focused on analysing the hydroelastic behaviour of very large flexible floating structures. However, since hydroelastic effects cannot be directly modelled using *ANSYS AQWA*, an established multi-body discretisation simplification was adopted. This approach involves connecting multiple rigid-bodies via connector joints with calibrated stiffness to approximate global structural flexibility. This is a commonly used simplification in offshore engineering for simulating flexible structures using potential-flow solvers like *ANSYS AQWA* [39,42]. Therefore using this technique for the FP archetype, a full-scale system with a total length of 300 m was discretised into 16 rigid bodies, each 18.35 m long, with 0.4 m gaps between adjacent floaters (see Fig. 3). These bodies were connected using hinge joints and four linear mooring lines were included in the setup, using similar properties to those in the LRP case due to the absence of specific mooring details in the reference studies. However, in this configuration, the mooring lines primarily serve to restrict drift and do not significantly affect the heave response of the system. A frequency statistical analysis was then performed for all five wavelengths reported in the reference studies. The heave RAOs for all floaters were then obtained at their respective centres of gravity, representing different locations along the full length of the structure for each of the five wavelengths, as shown in Fig. 4(d). As seen in the figure, the simulation results show good agreement with both the experimental and numerical reference data, with an overall RMSE range of 0.01–0.1 (m/m) across all five wavelengths and all reference studies. This confirms that the discretised configuration approach where the flexible structure is divided into several interconnected rigid bodies effectively replicates the dynamic behaviour of an FP-type archetype.

Additionally, to further quantify the deviation between the frequency–statistical analysis and the time-domain RAOs, a comparison was carried out for selected frequency points using the RP and LRP archetypes. The resulting overall RMSE values lie between 0.026–2.5 deg/m for pitch, 0.78–1.8 m/m for surge, and 0.011–0.25 m/m for heave. These RMSEs indicate that, in practice, the RAOs estimated from the time-domain simulations are reasonably consistent with those predicted by the frequency–statistical analysis (which were validated against the reference studies, as shown in Fig. 4). As the FP archetype follows the same hydrodynamic formulation as RP and LRP, and owing to the high computational time needed to reach steady state, the heave RMSE range obtained from RP and LRP can be used as a representative indication of the expected level of agreement for FP as well. For the LEP archetype, on the other hand, such a comparison was not performed because its validation is based solely on the RAOs obtained from hydrodynamic diffraction analysis in *AQWA*, consistent with the reference study; comparing these against time-domain RAOs would not represent the same physical configuration and would lead to an inconsistent assessment.

In summary, through this validation exercise, both unit archetypes and modular interconnected archetypes were verified against experimental and computational reference studies under both regular and irregular wave conditions, establishing strong confidence in the model's accuracy using *ANSYS AQWA* for OFPV applications. With the RAOs now validated from both frequency domain and time domain analysis, the hydrodynamic response package in AQWA is used to compute the actual time-series response across all six degrees of freedom, which forms the required hydrodynamic inputs for the subsequent steps in the modelling framework as shown in Fig. 2.

3.2. Orientation modelling

The second step in modelling the WIL involves translating the output of the hydrodynamic model i.e., the 6 DoF time-series response into tilt (θ_t) and azimuth (A_z) angles for use in the opto-electrical analysis as shown in Fig. 2. This step is essential for accurately determining the dynamic plane of array irradiance on each PV module based on its instantaneous orientation. As described in Section 3.1, the time-series response of a floating body is characterised by six degrees of freedom—three translational and three rotational. For calculating the module orientation, only the rotational degrees of freedom — roll (r_x), pitch (r_y), and yaw (r_z) are relevant, as they directly influence the plane of array irradiance, as illustrated in Fig. 5(a). The translational degrees of freedom, in contrast, are assumed to have negligible influence on plane of array irradiance due to the relatively small horizontal and vertical displacements involved. To estimate the plane of array irradiance, a hemispherical coordinate system is used in combination with the unit normal vector method. Every possible orientation of a PV module within this hemisphere can be represented by a unit outward normal vector, whose position can be fully defined by two angles: tilt (θ_t) and azimuth (A_z). Hence, to determine the (θ_t, A_z) of a module at each time step, it is first necessary to compute the coordinates of its corresponding unit normal vectors. However, extracting these coordinates directly is not straightforward, as the outputs from the hydrodynamic simulation

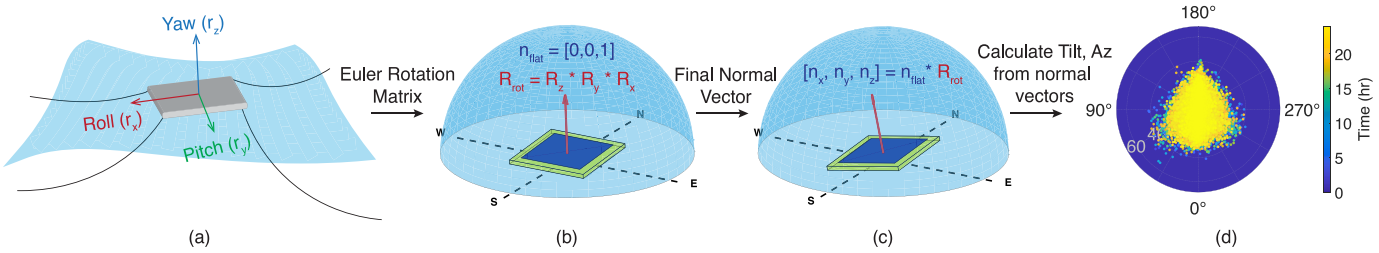

Fig. 5. Orientation modelling framework. (a) Results of the hydrodynamic time response analysis - 3 rotational degrees of freedom: pitch, roll and yaw are fed in (b) Euler's rotational transformation on the raw pitch, roll and yaw values, (c) obtaining the final normal vector of the floater and hence, (d) Variation of tilt and azimuth where the radial axis represents the tilt angle, while the angular axis denotes the azimuth angle, measured clockwise from South (0°). Each point is colour-coded by the time of day.

are the rotational degrees of freedom, which indicate how much the system has rotated (in degrees) about each coordinate axis. Therefore, an alternative approach is required to compute the coordinates of the normal vector corresponding to each orientation of the OFPV system.

To do this, we begin with a flat, horizontally positioned PV module represented by a unit normal vector of [0, 0, 1], which serves as the reference, as shown in Fig. 5(b). Then, the three-dimensional Euler rotation matrix is constructed based on the 3 DoF outputs from the hydrodynamic analysis as shown in Fig. 5(b). Finally, this rotation matrix is multiplied by the reference normal vector, as defined in Eq. (1), to obtain the resultant coordinates of the normal vector, as illustrated in Fig. 5(c). By performing this operation, the 3 DoF hydrodynamic responses are effectively translated into the coordinates of the normal vectors at each time step.

$$\begin{bmatrix} n_x & n_y & n_z \end{bmatrix} = \underbrace{\begin{bmatrix} 0 & 0 & 1 \end{bmatrix}}_{n_{\text{ref}}} \cdot \overbrace{\left(R_z \cdot R_y \cdot R_x \right)}^{R_{\text{rot}}}$$

$$\text{where: } R_x = \begin{bmatrix} 1 & 0 & 0 \\ 0 & \cos(r_x) & -\sin(r_x) \\ 0 & \sin(r_x) & \cos(r_x) \end{bmatrix} \tag{1}$$

$$R_y = \begin{bmatrix} \cos(r_y) & 0 & \sin(r_y) \\ 0 & 1 & 0 \\ -\sin(r_y) & 0 & \cos(r_y) \end{bmatrix}$$

$$R_z = \begin{bmatrix} \cos(r_z) & -\sin(r_z) & 0 \\ \sin(r_z) & \cos(r_z) & 0 \\ 0 & 0 & 1 \end{bmatrix}$$

Once the coordinates of the rotated normal vector at each time step is obtained, the corresponding θ_t, A_z angles are calculated using Eq. (2), following the reference convention $[S = 0°, W = 90°, N = 180°, E = 270°]$.

$$\theta_t = \tan^{-1}\left(\frac{\sqrt{n_x^2 + n_y^2}}{n_z} \right), \quad A_z = \begin{cases} 0 \text{ or } 360, & \text{if } n_x = n_y = 0, \\ \tan^{-1}\left(\frac{n_x}{n_y} \right) + 180, & \text{otherwise} \end{cases} \tag{2}$$

Hence, with this approach, the dynamic outputs from the hydrodynamic simulations can be effectively translated into corresponding time-varying θ_t, A_z values, which can then be used for the opto-electrical analysis—thereby bridging the hydrodynamic and opto-electrical simulation frameworks. Now that the dynamic values of θ_t, A_z are obtained, we can proceed to the next modelling step.

3.3. Opto-electrical modelling

The final step in calculating the WIL is to perform the opto-electrical analysis as shown in Fig. 2. For this purpose, the in-house developed modelling framework — the *PVMDtoolbox* is used. By default, the *PVMDtoolbox* supports cell-level to system-level modelling to predict the EY for Ground mounted PV systems [43,44]. In this work, its capability is further extended to model the EY of OFPV systems, with the methodology illustrated in Fig. 6. This flowchart outlines the overall opto-electrical modelling workflow, where the existing models are shown in blue, the intermediate outputs in green, the required inputs in black, and the additional models introduced in this work for simulating OFPV systems are shown in red. The working of this extended toolbox can be broadly explained in four stages which are as follows:

Stage 1: Optical Analysis (Steps 1–2): The simulation begins with an optical analysis, where ray-tracing is performed on the cell-layer stack to compute the absorption/generation profile. This generation profile is then used as input to an advanced semiconductor analysis model, which calculates the IV curves of the cell under varying irradiance and temperature conditions.

Stage 2: Hydrodynamic-Orientation Coupling (Step 3): The next step is the coupling of the hydrodynamic model with the *PVMDtoolbox* via the orientation model, as explained in Section 3.2. This coupling represents the first key addition introduced in this work. The output of this coupling is twofold: (a) the exact, time-resolved instantaneous orientation angles $(\theta_t, A_z)_{time}$, and (b) a discrete grid of orientations $(\theta_t, A_z)_{range}$ defined by the maximum and minimum angles as seen in $(\theta_t, A_z)_{time}$. This grid serves as a set of static snapshots representing the extremes and intermediate orientations (sampled at a specified step interval) within which all possible instantaneous responses of the system lie.

Stage 3: Plane of Array (POA) Irradiance (Steps 4–8): The next step is to calculate the plane of array irradiance and this is done by first decoupling the spatial and temporal effects. First, to account for spatial effects, the $(\theta_t, A_z)_{range}$, together with the absorption profile, PV module dimensions, and surrounding environmental conditions (shading and albedo), are used to generate a *sensitivity map (SM)*[2]. The SM quantifies how sensitive the module is to receiving irradiance from a particular part of the sky based on its orientation and surroundings. In a conventional approach, the SM would need to be recomputed for every instantaneous $(\theta_t, A_z)_{time}$ orientation during the dynamic response of the system, leading to computationally expensive frame-by-frame ray-tracing simulations. To overcome this limitation, the second key addition introduced in this work is the pre-generation of multiple SMs for all possible combinations of θ_t, A_z within the $(\theta_t, A_z)_{range}$ into a reference lookup matrix (steps 4–5, Fig. 6).

Next, to account for temporal effects, site-specific weather data (typically available at hourly or 10-minute resolutions) is used to compute the irradiance distribution across the sky dome via the Perez model to create a *skymap*[3]. A skymap defines how irradiance reaches the module over time as a function of the solar position. The third addition introduced in this work is the pre-generation of skymaps for every possible combination of $(\theta_t, A_z)_{range}$ to form a skymap lookup matrix (steps 6–7, Fig. 6). These two lookup matrices (the sensitivity map and

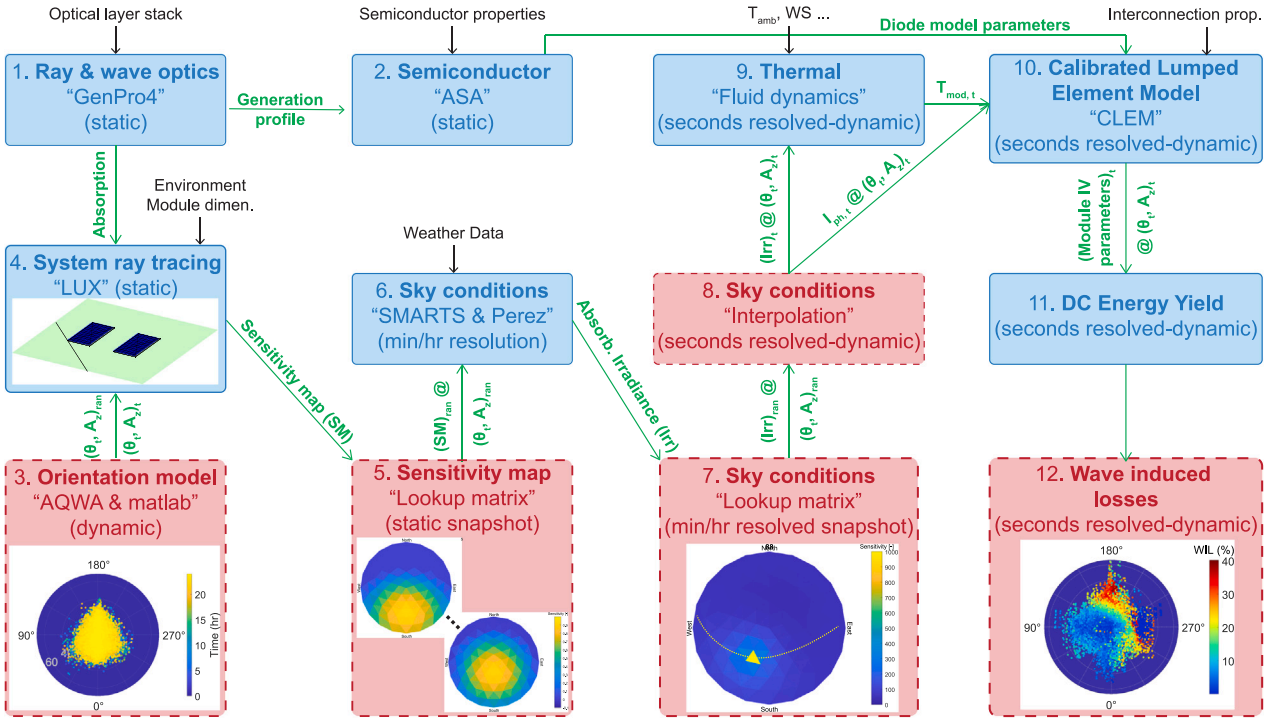

Fig. 6. Opto–electrical modelling framework. Elements shown in blue represent the existing modelling steps already incorporated in the PVMDtoolbox for modelling Ground mounted PV systems . Elements shown in red indicate the additions introduced in this work to enable the modelling of OFPV systems. Green arrows indicate the intermediate outputs, while the required inputs are shown in black.

the skymap) are then multiplied to estimate the POA irradiance lookup for every $(\theta_t, A_z)_{range}$ combination.

Finally, the fourth addition involves estimating the dynamic POA irradiance. To achieve this, a two-dimensional linear interpolation (using MATLAB's `interp2` function) is applied to every instantaneous $(\theta_t, A_z)_{time}$ orientation, using the precomputed static POA lookup tables as references. This step effectively transforms the static tables into a continuous, time-dependent POA irradiance signal (Irr_t) that evolves alongside the system's motion (step 8, Fig. 6). This approach preserves the accuracy of the POA outputs compared to the conventional workflow of the *PVMDtoolbox*, while saving orders of magnitude in computational time.

Stage 4: Electrical Conversion and WIL (Steps 9–12): Now by using (Irr_t), the module temperature $(T_{mod,t})$ is estimated[4]. Then, a lumped-element electrical model based on the one-diode equivalent circuit is used to compute the IV curves of the PV modules. The final output from this step is the DC power output at each time step, thereby accounting for the dynamic motion of the OFPV system (steps 9–11, Fig. 6). Finally, in the last addition, the WIL is computed using the DC power outputs obtained from step 11 through Eq. (3).

$$\begin{aligned}\text{WIL}\,(\%) &= \frac{P_{\text{ideal}}(t) - P_{\text{actual}}(t)}{P_{\text{ideal}}(t)} \\ &= \frac{\left[\sum_{i=1}^{N_{\text{panels}}} I_{\text{mpp},i}(t)\cdot V_{\text{mpp},i}(t)\right] - \left[I_{\text{mpp,min}}(t)\cdot \sum_{i=1}^{N_{\text{panels}}} V_{\text{mpp},i}(t)\right]}{\sum_{i=1}^{N_{\text{panels}}} I_{\text{mpp},i}(t)\cdot V_{\text{mpp},i}(t)} \times 100\end{aligned} \tag{3}$$

An additional algorithm is incorporated to account for the effects of bypass diodes, ensuring that the practical mismatch behaviour of the PV modules within the system is represented (step 12, Fig. 6). Therefore, up to this point, we have discussed how to model the hydrodynamic behaviour of different archetypes and validated their responses, followed by the conversion of the hydrodynamic outputs into $(\theta_t, A_z)_{time}$. Finally, we outlined the extensions made to the *PVMDtoolbox*, enabling it to account for wave-induced effects on EY. With these additions, the toolbox now stands as one of the few modelling frameworks capable of calculate WIL for OFPV systems.

While the proposed approach is robust and performs well under different operating conditions, a couple of inherent modelling challenges still remain that need to be addressed to further strengthen the modelling framework. The first challenge pertains to the **long-term response prediction**. To estimate WIL over weeks, months or years, the hydrodynamic motions of the system must be known over the same duration. However, directly simulating such long time-series in *AQWA* is computationally infeasible. To address this, a long-term response reconstruction method is proposed, where a short (10 min) *AQWA* simulation is statistically extended to longer durations while still preserving the essential motion characteristics and WIL accuracy. To ensure the reliability of this strategy, the method was rigorously validated through a series of stress-tests designed to validate its performance under certain worst-case scenarios as detailed in Section S3.1 of the supporting information. The results demonstrate that the difference in WIL obtained using direct *AQWA* responses compared to the response derived using the proposed method is less than 0.2% over a 24-hour simulation period. This confirms that the proposed method can reliably and accurately represent long-term system behaviour for the purpose of estimating WIL while significantly reducing computational demand (further details can be found in Section S3.1 of the Supporting Information).

The second challenge concerns the choice of an appropriate **time-step resolution** for the reconstructed long-term response. By default, *AQWA* outputs motion time-series at a fine temporal resolution (ΔT = 0.1 s), which makes the subsequent opto–electrical modelling for long-term periods highly computationally demanding. To address this, a time-step sensitivity analysis was conducted (details in Section S3.2 of the supporting information) to compare how different time-step resolutions (ranging from 0.1 s to 10 min) affect the WIL. The results showed that a resolution of ΔT = 60 s provides an optimal balance between

accuracy and computational efficiency. At this resolution, the RMSE of the WIL is less than 0.35% compared to the results using the default fine resolution of 0.1 s. While the optimal resolution (ΔT = 60 s) may not track every individual oscillation of the system, it does not significantly impact the WIL results as shown in Section S3.2 of the supporting information. This is because, from a practical standpoint, sub-second or sub-minute WIL profile is rarely used in real-world applications, which typically rely on hourly, monthly, or yearly profiles. Since this work aims to estimate hourly WIL which is an integrated metric, the finer level oscillations missed by the 60 s time step effectively average out over the hour maintaining reliable WIL projections comparable to those obtained with much finer resolutions. Therefore as a result of this sensitivity analysis, a time step of 60 s is used consistently throughout the remainder of this work.

With these two challenges now resolved, the modelling framework is now capable of generating long-term, physically consistent WIL estimates with practical computational effort thereby answering the first research question **RQ1**.

4. Sensitivity analysis

Up to this point, the modelling framework and the associated challenges were addressed for calculating the WIL. The next step is to quantify the WIL and to investigate how different geometrical and environmental based parameters influence WIL thereby addressing **RQ2.** on *How to comprehensively quantify WIL through a multi-parameter (geometrical + environmental) sensitivity analysis across diverse OFPV archetypes?* To address this, a comprehensive sensitivity analysis is conducted by systematically varying both design- and environmental-based quantities. In this section, the methodology of the sensitivity study is first introduced, followed by the design of the simulations and lastly the resulting WIL profiles from each case study are presented to highlight the key parameter dependence patterns.

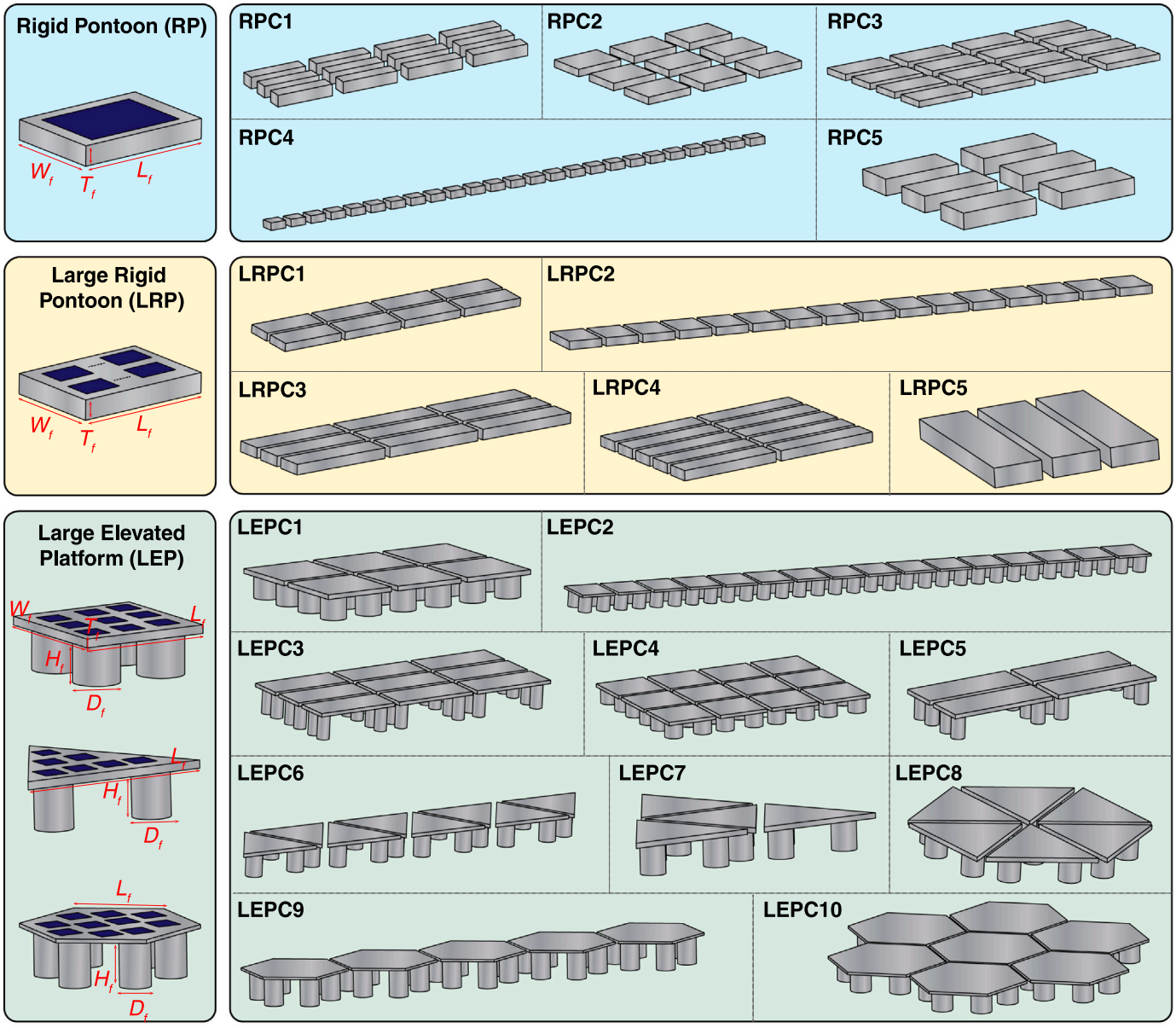

Fig. 7. Unit archetype designs and farm-level variations forming the geometrical design of the simulation cases. The nomenclature here aims to define the base cases used in study which follows the structure "base design" (RP/LRP/LEP) followed by "Cx", where "Cx" denotes the case number within that specific floater design category. Note: The designs formulated in this study are inspired by practical deployments but are not intended to represent or correspond to any specific organisation's proprietary design; they serve only as generic representations.

4.1. Methodology for design of simulations

The objective of the sensitivity analysis is to quantify how wave-induced losses (WIL) depend on both design choices and environmental conditions. To define a robust parameter set, we use the modelling chain introduced in Section 3 as a reference to identify which inputs directly affect the WIL. Accordingly, the category of parameters selected for variation are — unit archetype geometry, farm layout, connector and mooring properties, sea-state characteristics, and solar conditions. These particular categories were chosen because they are the primary levers that govern platform motions and, through the orientation–irradiance coupling, the magnitude and variability of WIL.

Next, to construct the sensitivity-analysis sample space, a full factorial approach is typically employed. However, in this case, it is impractical because there are large number of tunable parameters which would lead to a prohibitively large number of simulation runs and, consequently, infeasible computational cost. We therefore employ Latin Hypercube Sampling (LHS) approach using the MATLAB `lhsdesign` function [45]. LHS stratifies each parameter range into equiprobable intervals and draws one sample from each interval, providing near-uniform coverage of the multidimensional design space while avoiding redundant combinations. This approach therefore yields a well-distributed set of simulations with a manageable number of runs, enabling the subsequent sensitivity analysis and quantification of WIL at acceptable computational cost.

Finally, before performing the sensitivity analysis, a set of modelling assumptions is intentionally enforced across all cases: PV module temperature is held constant at 25 °C, shading effects are neglected, only rigid-body archetypes are considered, waves are assumed long-crested, and the wave spectrum is treated as stationary over each simulation duration. These assumptions ensure that variations in WIL are attributed solely to changes in the design and environmental parameters under investigation, rather than to confounding thermal or shading effects.

4.2. Design of simulations

The first step in the sensitivity analysis is to define the design of the simulations. This involves specifying the geometry, connector, mooring, and environmental properties, which are detailed in the following subsections.

4.2.1. Unit archetype and farm parameters

The geometrical configuration is determined by varying the system design parameters, which are grouped into two categories: unit–archetype design parameters and farm-level design parameters.

(1) Unit archetype design parameters: For this sensitivity study, three different types of archetypes are considered as shown in Fig. 7 — the rigid pontoon (RP), where each pontoon supports one PV module; the large rigid pontoon (LRP), where each pontoon supports multiple PV modules; and the large elevated platform (LEP), which consists of multiple cylindrical legs and a deck capable of supporting multiple PV modules, as shown in Fig. 7. Each unit archetype can be defined by a set of geometrical parameters such as the length of the pontoon or deck (L_f), width of the floater or deck (W_f), thickness of the pontoon or deck (T_f), height of the cylindrical leg (H_f), diameter of the cylindrical leg (D_f), and number of sides for the deck (n_{sides}). These geometrical parameters are determined based on the number of PV modules (N_{PV}) that each floater needs to accommodate. Once the geometrical dimensions are defined, the mass of each unit archetype is computed using the mass of each PV module (m_{PV}) and the floater material density (more details in Section S4 of the Supporting information) via the density (ρ)–volume (vol) relationship ($\rho = mass/vol$) in *MATLAB*. The corresponding draft (depth of the floater below the waterline) of the system is then calculated using the Archimedes' principle, and the moments of inertia (and radii of gyration) about the global axes are determined using *SolidWorks* [46].

(2) Farm design parameters: With the unit archetype design fully defined, the next step involves varying the farm-level parameters. To construct the farm, the unit archetypes are arranged in a modular grid pattern governed by three main factors: the gap between adjacent floaters (gap), the total number of floaters in the farm (N_f), and the number of rows and columns in the configuration (M_{row}, N_{col}). The number of floaters and the overall farm layouts are determined through iterative trials to ensure computational feasibility and hydrodynamic stability of the system. The gap between floaters on the other hand is systematically varied by taking the RP validation study (which used a 0.15 m gap) as reference for all other archetypes, with proportional increases or decreases applied based on their respective dimensions and design scales.

All in all, the overall geometrical parameters varied in this study are : L_f, W_f, T_f, H_f, D_f, gap, N_f, and M_{row}, N_{col}. As a result of these variations, the total mass of the unit archetype (M_{tot}), draft, and radius of gyrations (k_{xx}, k_{yy}, k_{zz}) also change accordingly. Using the LHS method, a total of 20 different base cases (where each base case corresponds to a different floater assembly) are formulated by varying the above parameters, consisting of 5 unique RP, 5 unique LRP, and 10 unique LEP designs as shown in Fig. 7. The complete geometrical design of simulations is summarised in Section S4 of the supporting information.

4.2.2. Connectors and mooring line parameters

The next step is to determine the parameters related to the interconnectors and mooring lines. In this study, a ball-and-socket type interconnectors and linear mooring lines are used for all cases. Both connectors and mooring lines have specific parameters that need to be varied for each base case. For the connectors, these include the rotational stiffness across the three axes (R_x, R_y, R_z) and the rotational damping across the three axes (C_x, C_y, C_z). For the mooring lines, the key parameters are the length of the mooring lines (L_{moor}), stiffness of each line (K_{moor}) and the pretension in the lines (PT_{moor}) (definition in Section S1 of the supporting information). As the purpose of this study is not to design the connectors or mooring systems in detail, but rather to understand how their variations influence WIL, a simple scaling–based approach is adopted instead of assigning arbitrary or fixed values to these parameters for each case. This approach, detailed in Section S5 in the supporting information, provides a physically consistent and repeatable framework that links each case to its corresponding validated reference configuration. As a result, the connector and mooring properties evolve logically with changes in system geometry and layout, ensuring consistent and logical variation of the above mentioned parameters across all simulations. The connector and mooring properties used for each base case are summarised in Section S5 in the supporting information.

4.2.3. Environmental parameters

Now that the different unit archetype, farm-level, interconnector, and mooring line properties have been defined and varied, the next step is to determine the environmental properties. To vary the environmental conditions, the following properties need to be determined: (1) wave properties and (2) solar properties.

(1) Wave properties: To define the wave conditions, two locations are considered in this work: one near the North Sea and one near the Great Australian Bight, as shown in Fig. 8(a, e). For both locations, the hourly wave properties are extracted using the ERA5 global reanalysis dataset [47]. Parameters such as water depth (26 m in the North Sea and 1000 m in the Great Australian Bight), significant wave height (H_s), and peak wave period (T_p) for the entire year of 2024 are extracted, as shown in Fig. 8(b, f). These plots show the probability of different H_s–T_p combinations throughout the year, offering an overview of the sea state characteristics and their relative occurrence. From these plots, it can be noticed that for instants when the waves are

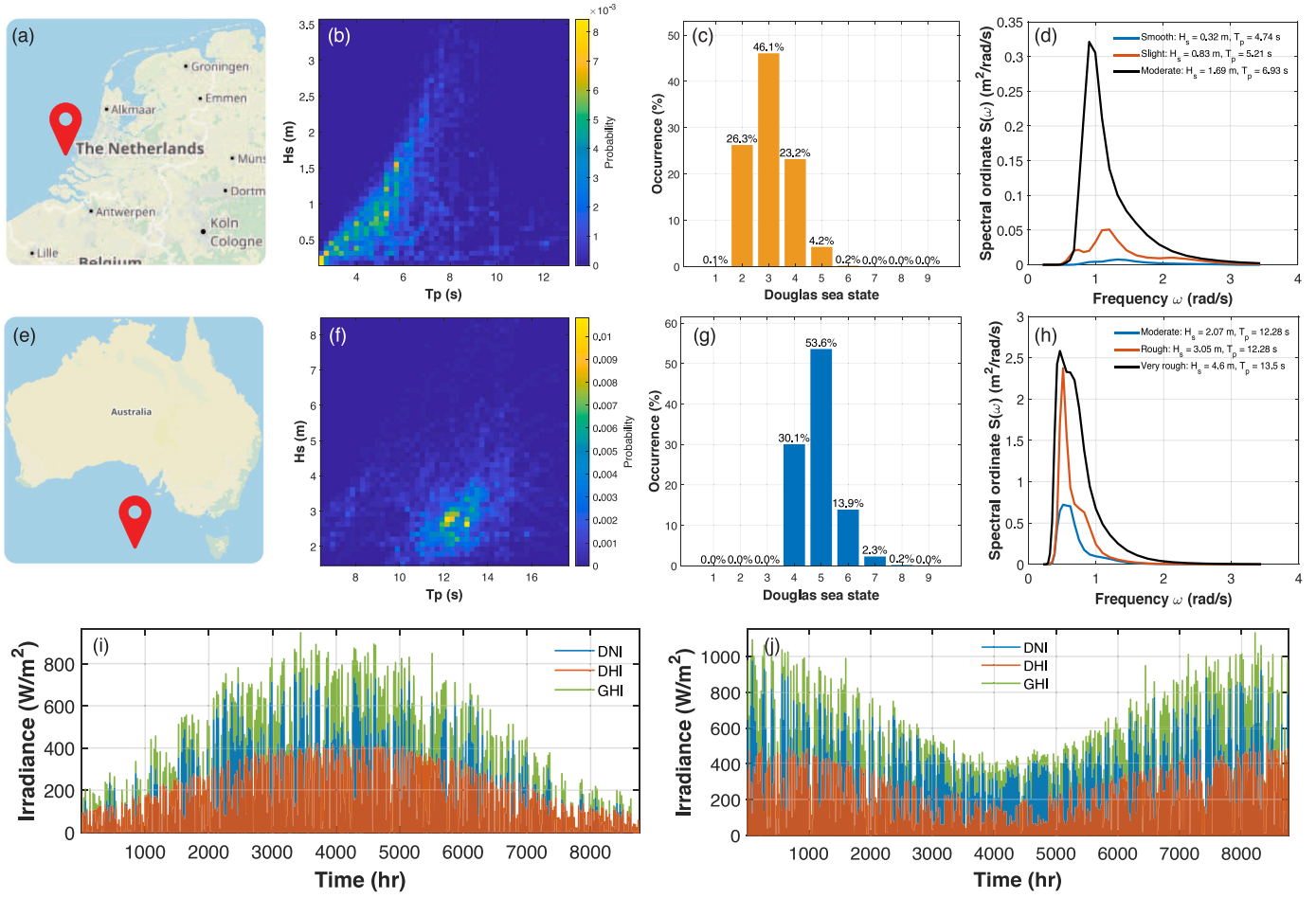

Fig. 8. Location dependent design of simulations. (a, e) Two different locations selected for the sensitivity analysis, (b, f) The probability of Hs and Tp occurrence at both the selected location for the year of 2024, (c, g) the most probable sea state at both the location for the entire year of 2024, (d, h) The representative sea state spectra for both locations with the 3 most occurring sea states. (i, j) the DNI, DHI, GHI profiles for the entire year at both locations.

tall (high H_s), the wave is usually a long (medium to low T_p) and vice versa.

To use this real-world data in the hydrodynamic simulations, it must first be converted into a wave spectrum that defines the energy that the waves carry for different frequencies. In order to calculate that, first the extracted hourly H_s are categorised according to the Douglas sea state classification (for example, sea state 2 is termed as 'smooth' when the H_s lies between 0–0.1 m and sea state 6 is termed as 'very rough' when H_s lies between of 4–6 m) [48], and the probability of occurrence for each sea state is plotted for both locations, as shown in Fig. 8(c, g). From both the plots, it can be observed that the most commonly occurring Douglas sea states are: 2, 3, and 4 in the North Sea and 4, 5, and 6 in the Great Australian Bight. Together, these six sea states represent approximately 95% of the wave conditions at both the locations for the period of 2024. Now that we know the most probable sea state at each location, the next step is to determine the corresponding (H_s, T_p) pair for each sea state. To do this, the representative H_s is first computed by taking the mean of all hourly H_s values that fall within the H_s range defined by the Douglas classification for that sea state (for example, when H_s lies between 4–6 m, it belongs to sea state 6, and the representative mean H_s for sea state 6 is obtained by averaging all hourly H_s values within 4–6 m). Once this mean representative H_s is obtained, the corresponding T_p at this mean H_s is extracted from the same hourly ERA5 dataset. This procedure yields the representative (H_s, T_p) pair for each of the six sea states as shown in Fig. 8(d, h).

Next, the 2D wave spectrum $(S(\omega_i, \theta_j))$ at each of the (H_s, T_p) combination for all the six sea states are extracted from ERA5 which provides the wave energy (S) as a function of frequency (ω_i) and directional spread (θ_j). In this study, a long-crested wave assumption is made, meaning that the entire energy of the wave propagates from a single dominant direction. Hence, this 2D spectrum which also includes the directional spread needs to be converted to a 1D spectrum which only varies as a function of frequency (ω_i). To obtain this 1D spectrum, the 2D spectrum is integrated over all directions using Eq. (4). This process is repeated for all six sea states to derive their respective 1D spectra, as shown in Fig. 8(d, h).

$$S_{1D}(\omega_i) = \int_{j=1}^{n_\theta} S_{2D}(\omega_i, \theta_j)\, d\theta \tag{4}$$

(2) Solar properties: With the wave properties now defined, next we need to estimate the solar properties at the selected two locations. Both these locations are chosen deliberately as they allow for variation in solar path characteristics across different hemispheres — one site in the northern hemisphere and one in the southern. For both locations, solar irradiance data are extracted using Meteonorm 7.2 [49], as shown in Fig. 8(i,j). Meteonorm naturally does not host solar property databases for offshore locations, however it interpolates between multiple nearby ground weather stations and satellite weather data to estimate the solar properties at each of the selected offshore sites making the resulting dataset is sufficiently reliable for the purpose of this sensitivity analysis.

In summary, the environmental parameters varied in this study include significant wave height (H_s), peak wave period/ wavelength

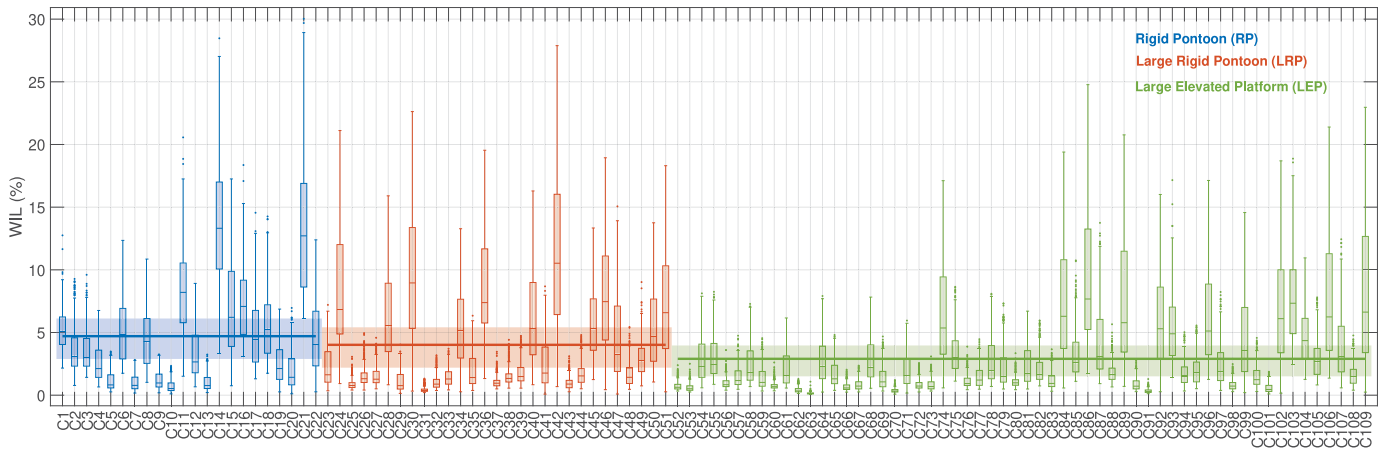

Fig. 9. The hourly WIL profile for the 109 simulations (C1, …, C109) formulated as part of the sensitivity analysis. The nomenclature "Cy" refers to an individual simulation case (within the 109 simulations), as defined in the main text. Further details on how each simulation corresponds to its respective base case and sea state can be found in Section S6 of the supporting information.

(T_p, L_p), wave spectrum ($S(\omega_i)$), wave direction (θ_{wave}), solar azimuth ($A_{z,\,sun}$), solar altitude (h_{sun}), direct normal irradiance (DNI), diffuse horizontal irradiance (DHI), and global horizontal irradiance (GHI). With the 20 base cases (see Fig. 7) defined in the previous section, each base case assembly is simulated under all six representative sea states, resulting in a total of 120 simulations. Out of these 120 simulations, *AQWA* terminated 11 simulations with the error message "the ratio of distance change exceeded 75%", indicating that the relative motions became too large for the solver to maintain a consistent articulation configuration due to an unstable response at that particular sea state. Most of these unstable simulations occurred for the RP and LRP archetypes under sea state 4 in the North Sea or sea states 5/6 in the Australian Bight, which correspond to rough conditions according to the Douglas classification. As a result, these 11 simulations were removed from the final list of simulations thereby forming a total of 109 simulations for the sensitivity analysis.

4.3. Results

Now that the 109 simulations forming the sensitivity analysis have been fully defined, for each of these simulations a one-month EY analysis is performed at both the locations. A one-month simulation is performed to keep the computational effort within practical limits. Additionally, the choice of the selected months depend of the location where the system is placed. When the system is located in the North Sea, the selected month is July, while when the system is placed in the Great Australian Bight, the selected month is December.

In both cases, a summer month with relatively higher irradiance is selected to capture a wider range of plane-of-array irradiance variability, as summer periods generally exhibit a broader spread of DHI and DNI values than winter (aimed at having a larger spread for the surrogate model as explained in the next section). Although winter months may feature larger floater motions due to higher H_s, WIL is governed not only by motion-induced orientation changes but also by the plane-of-array irradiance. Importantly, the irradiance levels encountered in winter naturally lie within the broader irradiance envelope observed in summer; thus, selecting a summer period here does not necessarily underestimate the WIL in the winter periods.

Now that we have all the input parameters needed, the overall workflow is as follows: First, the unit archetype design is defined as per Section 4.2.1. Then, a farm topology is created using this unit archetype configuration, following Section 4.2.1 forming the 20 base cases. Next, the connector and mooring line properties are varied for each base case according to Section 4.2.2. Then, six hydrodynamic simulations are performed for each base case (corresponding to the six sea states considered — three in the North Sea and three in the Australian Bight; in total, 20 base cases × 6 sea states = 120 simulations, out of which 109 remain after filtering). From each simulation, the tilt and azimuth responses of every floater are computed for the entire one-year duration using a time step of 60 s, based on the statistical–correction RAO approach described in Section S3 of the supporting information. For each of these simulations, a one-month EY analysis is then performed using the PVMDtoolbox as per Section 3.3. Since only a one-month EY simulation is considered, the tilt and azimuth values corresponding specifically to the selected months (July and December) are extracted from the annual response. This ensures that the orientation response and the irradiance inputs used for the EY calculations correspond to the same months, thereby maintaining full temporal consistency when computing WIL.

This process is then repeated for all 109 simulations, and the overall results of the sensitivity analysis are presented in Fig. 9. This figure shows the hourly variation of WIL as a function of the 109 simulation cases, sorted in ascending order of wave steepness (H_s/L_p, calculated from the sea-state conditions) for each archetype (further details on how each simulation corresponds to its respective base case and sea state can be found in Section S6 of the supporting information). Several key observations can be drawn from this plot. (1) The individual boxplots show that WIL distributions are widely spread with limited clustering, reflecting strong temporal variability caused by wave and irradiance fluctuations. The RP and LRP simulations show roughly 40%–45% of cases with high spread, compared to only about 20%–25% in the LEP archetype. This suggests that the LEP configuration generally demonstrates more stable dynamic behaviour under varying environmental conditions. However, this is just a general trend. Certain LEP cases (e.g., C86 and C109) display a spread comparable to RP and LRP cases. This indicates that the interaction between a specific system configuration and local environmental conditions plays a vital role in determining the most viable design for a particular location. Ultimately, this also suggests there may be no single "winner" design that performs consistently well under all operating conditions.

(2) When examining the dependency of WIL on H_s/L_p, a general upward trend can be observed i.e. WIL increases as H_s increases. This is logical as steep waves forces the floaters to tilt more aggressively to follow the surface profile, which lead to higher angular mismatch between modules. However, this trend does not always hold, as several outliers (e.g., C6, C30, C74) deviate from this behaviour. This indicates that the dependency of WIL on H_s/L_p is nonlinear and is most likely also influenced by other geometric and solar parameters and cannot be simply explained by structural, wave, or solar characteristics in

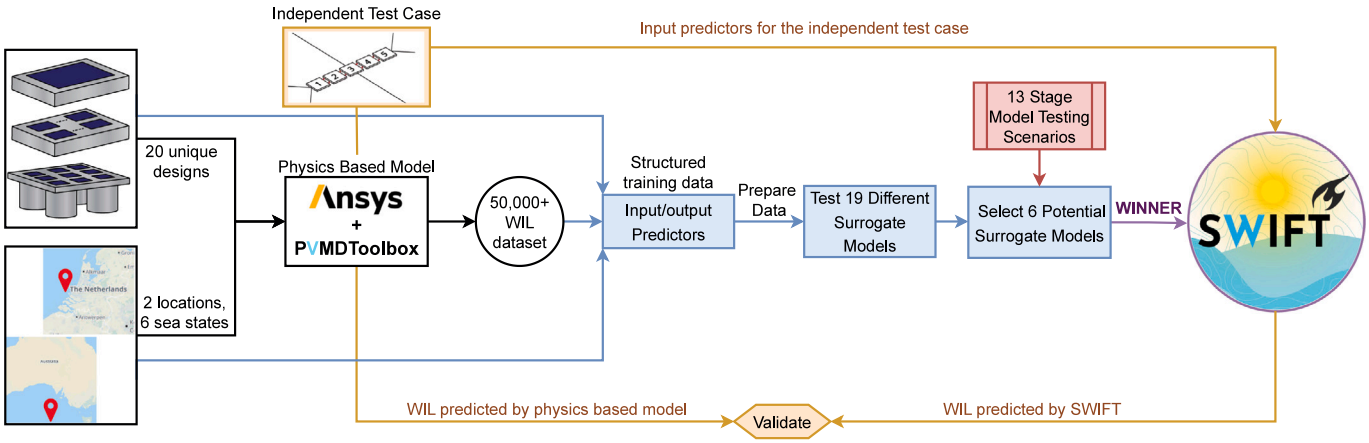

Fig. 10. The surrogate model development methodology.

isolation. (3) The plot also shows a mean of all hourly WIL values per archetype (solid lines) and a mean interquartile area bounded by the averaged 25th and 75th percentiles ($P_{25,avg}$ = mean($P_{25,RP/LRP/LEP\ cases}$) and $P_{75,avg}$ = mean($P_{75,RP/LRP/LEP\ cases}$), respectively). On average, it can be noted that the RP archetype exhibits hourly WIL between 3%–6%, LRP between 2.2–5.5%, and LEP between 1.5%–4%, indicating that the LEP archetype generally yields the lowest average hourly WIL. However, this does not necessarily say that the LEP is the best-performing configuration under all operating conditions. This is because, when the interquartile shaded areas are carefully examined (see Fig. 9), certain areas of overlap can be observed across the three archetypes. From this, it becomes clear that each archetype can technically outperform any other under certain conditions. This further reaffirms that no single design or environmental parameter solely dictates the overall WIL behaviour.

Overall, the results of this sensitivity analysis provided a broad quantitative characterisation of WIL across a wide range of geometries, operating conditions, and sea states, thereby addressing the second research question **RQ2**. However, the large spreads and cross-archetype overlap demonstrate that WIL is not governed by a single driver but instead emerges from a nonlinear interaction between multiple coupled design-level and environmental parameters. These interactions cannot be disentangled by direct inspection of individual simulations alone (which could be a side-effect of using the LHS method), as the inter-dependencies of WIL cannot be extracted in a straightforward manner. Therefore, a model capable of capturing this nonlinear behaviour is required to gain a deeper understanding of the physical mechanisms driving WIL.

5. Surrogate modelling

In this section, we build on the findings of the sensitivity analysis, which showed that WIL arises from coupled and highly nonlinear interactions between multiple design and environmental parameters. To better understand these dependencies and to generalise the behaviour beyond the analysed cases — a data-driven surrogate modelling approach is adopted. The overall workflow used to develop, test, and validate the surrogate model is shown in Fig. 10.

A surrogate model can be defined as a data-driven machine learning method that learns the relationship between the input parameters (geometrical, mechanical, and environmental) and the resulting WIL. This approach is particularly well suited for this work, since the results of the sensitivity analysis produced a large and diverse dataset of simulated WIL values that can be used to train the model as shown in Fig. 10. The trained surrogate model can therefore be used for two main purposes: (1) to provide a predictive framework capable of forecasting WIL for new design configurations or operating conditions without performing computationally expensive hydro–opto–electrical simulations thereby addressing **RQ3.** on *How to formulate a computationally efficient, data-driven surrogate model to predict long-term WIL for different designs and operating conditions?*, and (2) to better understand the non-linear behaviour and to quantify the key factors influencing WIL.

To develop a reliable surrogate model, we follow four main steps, as outlined in Fig. 10 which are — assembling the input dataset, defining the input–output predictors with an initial model screening, training and testing potential candidate models, and validating the selected final model. The process begins with the generation of a comprehensive training dataset, which is derived directly from the physics-based sensitivity analysis as shown in Fig. 10. In the following subsections, we detail the subsequent three steps (highlighted in blue, red, and orange in Fig. 10) required to construct and verify the surrogate model.

5.1. Data preparation and initial model screening

The first step in developing a surrogate model is the preparation of the input–output dataset as shown in the first blue box of Fig. 10. The predictive capability of any surrogate model is only as strong as the data it is trained on. Since the goal here is for the model to learn the non-linear dependencies and potentially forecast the WIL, it is essential that the input predictors are carefully formulated based on the governing physics of the problem. This is because a surrogate model simply "sees" the input predictors as numbers that influence the output (i.e., the WIL values), it has no inherent physical understanding and treats the data purely from a mathematical standpoint. Therefore, it is the responsibility of the user to supply predictors that truly influence the WIL. Only then the surrogate model can learn the correct dependencies rather than fitting spurious or coincidental correlations.

Therefore, in this study, a total of 32 input predictors are formulated, as summarised in Section S7 in the supporting information. These predictors form a balanced set covering unit archetype design parameters, farm-level parameters, interconnection properties, mooring properties, as well as environmental descriptors (wave and solar). This comprehensive combination enables the model to capture the complex nonlinear interactions observed in the simulations (see Fig. 9). To ensure that all predictors contribute uniformly during model training, each input parameter is normalised using the min–max scaling method described in Eq. (5). This scaling confines all predictors within a common range of [0, 1], preventing numerical bias towards variables with larger magnitudes and reducing the likelihood of overfitting or underfitting depending on the surrogate model type, thereby improving the overall training process.

$$\chi_{scaled} = \frac{\chi_{true} - \chi_{min}}{\chi_{max} - \chi_{min}} \tag{5}$$

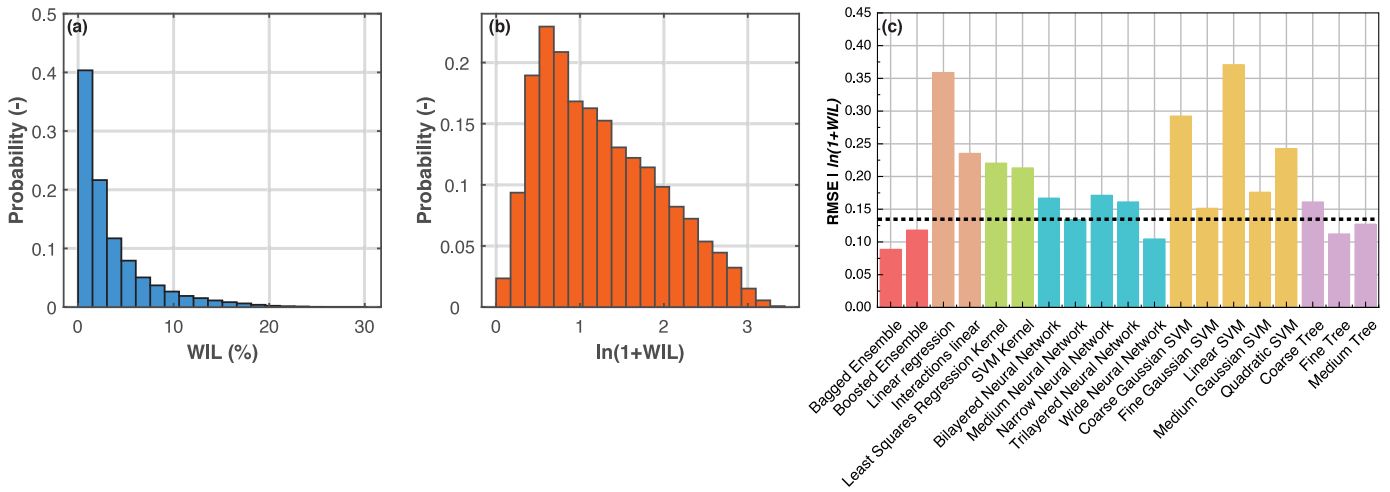

Fig. 11. Probability distribution of hourly WIL datapoint across all simulations and initial surrogate model screening. (a) true WIL distribution, (b) natural logarithmic distribution, (c) initial screening and comparison of different surrogate models.

Now that the input dataset is prepared, the next step is to prepare the output dataset for training, which is the *WIL*. The raw values of WIL cannot be directly used for training as they exhibit a long-tailed distribution with a few instances of high WIL values, as shown in Fig. 11(a). Such a distribution with skewed data can bias the training process, as the model may underemphasise these infrequent yet physically meaningful events. To mitigate this effect, the output variable is transformed using the natural logarithm of $(1 + WIL)$, as illustrated in Fig. 11(b). This transformation smoothens the low-probability occurrences of extreme WIL values while still preserving their relative differences. Doing this thereby improves the model's overall sensitivity to capture such rare events across the full WIL range. In addition to this, data points corresponding to $mean(POA_{all\ floaters})_{time} \cong 0$ where POA is the plane of array irradiance are excluded from the dataset, as they represent sunrise and sunset periods where WIL has no physical meaning. This ensures that the model is trained only under conditions where non-zero WIL can physically occur.

After processing the input and output data, the complete dataset consisting of *53,962* WIL datapoints across all 109 simulations was used to train different surrogate models from five main families available within MATLAB's `Regression Learner` as shown in the second blue box of Fig. 10: Ensemble Tree methods, Linear Regression, Kernel-based methods, Neural Networks, Support Vector Regression (SVR), and Decision Trees (further details on these models can be found in [50]). This initial screening step was performed to identify which algorithms is/are most suitable for capturing the nonlinear behaviour of WIL.

All the models from each family were trained on the full set of *53,962* datapoints using a five-fold random cross-validation method (further details on this will be discussed in the upcoming section). The prediction of each model was then compared against the true $\ln(1 + WIL)$ response, and their performances were evaluated using the Root Mean Square Error (RMSE, more information on why RMSE is chosen as the metric of comparison can be seen in Section S9 of the supporting information), as shown in Fig. 11(c). From this plot, several observations can be made: (1) linear regression models exhibit high RMSE and are therefore unsuitable, which is not surprising and simply reinforces the non-linear nature of WIL; (2) SVMs and kernel-based methods also perform poorly, as indicated by their relatively high RMSE values; (3) in contrast, Ensemble models, Neural Network models, and Decision Trees perform noticeably better with lower RMSE, suggesting their ability to capture the non-linear behaviour of WIL more effectively; and (4) since no single model is an evident overall winner in terms of predictive power, the best-performing models i.e., those with RMSE below the black dotted threshold in the plot — were shortlisted for further testing as shown in the third blue box of Fig. 10.

5.2. Training and testing the model

Now that we have multiple models with a low RMSE in the initial screening test, the next question that naturally arises is: *which model should be selected to predict WIL most reliably?* The answer to that is, while the initial screening (see Fig. 11(c)) provides a first indication of the most promising surrogate model algorithm, it does not fully capture the model's robustness under different testing conditions. What this means is that, in the initial model screening, the models were evaluated using a random 5-fold cross-validation technique. In this approach, the entire training dataset is first randomly divided into five equal subsets. The model is then trained on four of these subsets and tested on the remaining one. This process is repeated five times so that each subset serves once as the validation fold. The final accuracy is then calculated as the average performance across all five iterations. Although this method provides a general measure of predictive accuracy, it can overestimate model performance when internal correlations exist within the dataset.

What this means is for instance in this study, each of the 109 simulations contributes to roughly 500 hourly WIL values (excluding periods when $mean(POA_{all\ floaters})_{time} = 0$). As a result, data points from the same configuration (base case–sea state–location combination) may appear in both the training and testing sets, allowing the model to encounter nearly identical samples during validation. Due to this, the model tends over inflate the fit with the true data thereby showing an over-optimistic RMSE. Therefore to avoid this *hallucination*, a more comprehensive validation approach is required to assess how well each model truly generalises the WIL.

To achieve this, a comprehensive 13-stage validation framework was developed in this work (outlined in Section S8 in the supporting information) to further test the shortlisted models from the initial screening as shown in the red box in Fig. 10. The motivation behind this stage-wise validation is that each stage isolates a specific physical aspect of the problem to assess how well the model can generalise variations in sea state, location/irradiance, and geometrical configuration. This approach allows evaluation of the model's ability to interpolate within its training domain and, where possible, extrapolate beyond it. This structured testing procedure quantifies not only the model's predictive accuracy but also the boundaries within which it can be reliably used, thereby revealing the true predictive performance of each selected model.

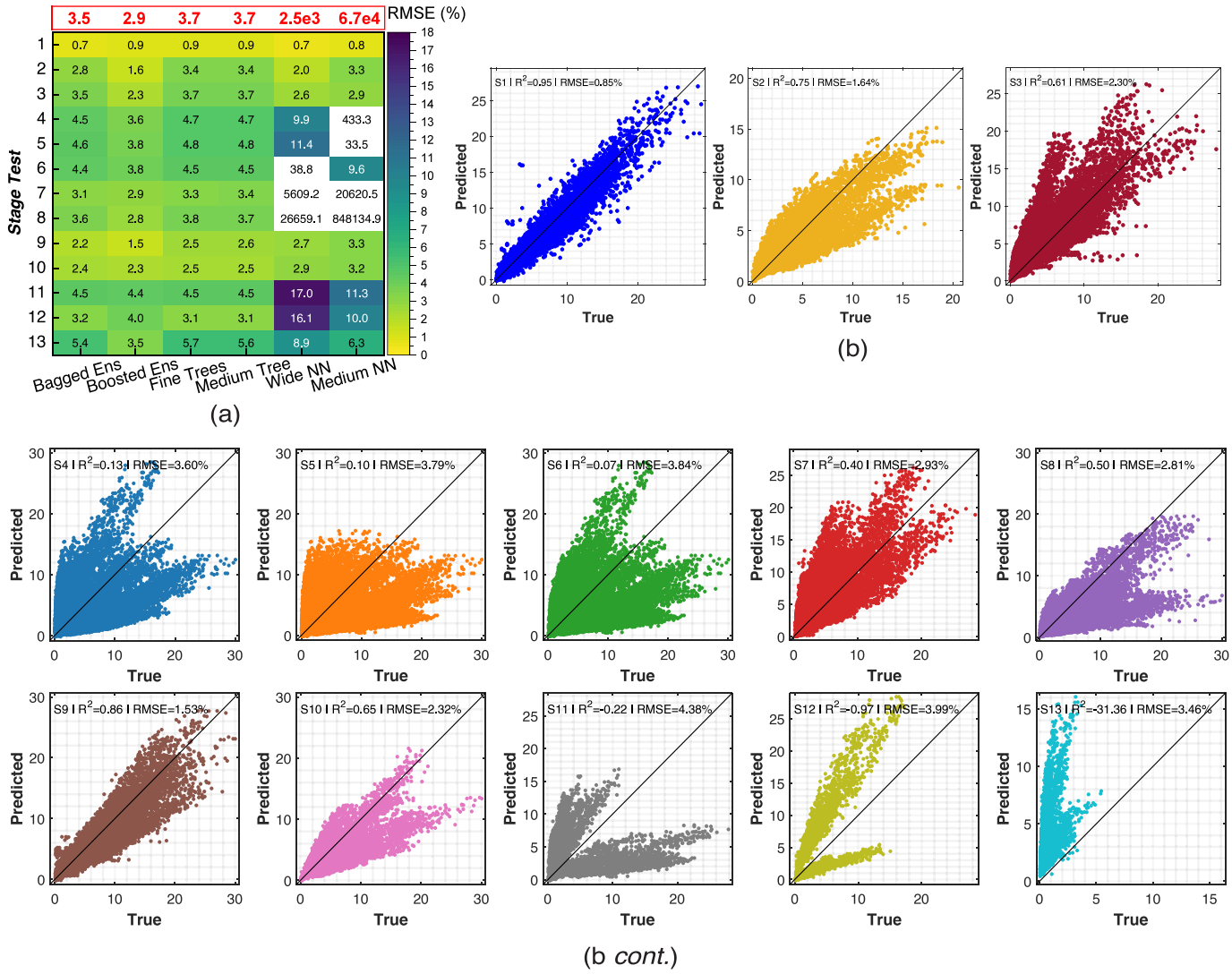

Fig. 12. Stage testing validation results. (a) Comparison of different surrogate models based on RMSE calculated from hourly WIL data, and (b) comparison between predicted and true WIL values (both in %) obtained using the boosted ensemble surrogate model for all the 13 validation stages. (Performance metrics used in this work can be referred to Section S9 in the supporting information.)

Fig. 12(a) shows the results of the 13-stage validation, where the performance of each selected model is quantified by comparing the RMSE of the predicted values against the true WIL values (converted to original units, %) for each stage. From the plot, the following observations can be made: (1) models such as the default wide and medium Neural Network models, although they exhibited a low RMSE in the initial screening test, fail to maintain this accuracy across several validation stages. This indicates that their earlier performance was driven by over-optimistic cross-validation rather than true generalisation capability, deeming that the default neural network frameworks are unsuitable for predicting WIL; (2) the Decision Tree models on the other hand show a reasonably good predictive performance across all stages, with a few high RMSEs in stages designed to test extrapolative capability of the model, but their overall average RMSE across all stages (see the top red box in Fig. 12(a)) is still comparatively higher than that of the ensemble models ; and (3) among all the selected model families, the ensemble models exhibit the strongest generalisation capability, consistently yielding the lowest average RMSE. Although the bagged ensemble achieved a slightly lower RMSE than the boosted ensemble in the initial screening, results of the 13-stage validation shows that the boosted ensemble performs more reliably across all validation stages and achieves the lowest RMSE overall.

The detailed performance of the Boosted Ensemble model used in this study configured with a minimum leaf size of 5, 1200 learning cycles, and a learning rate of 0.03 is shown in Fig. 12(b), where the predicted and true WIL values in % (not $ln(1+WIL)$) are compared for each stage test. For most stages, the predictions align closely with the $x = y$ line, indicating a strong overall fit. Noticeable deviations occur mainly in the extrapolation stages, particularly when geometric configurations lie outside the trained range (S11–S13, see Section S8 in the supporting information) which represent some of the most challenging tests for a surrogate model. Under these conditions, two visible clusters appear in stages S11–S13 as seen in Fig. 12(b). These clusters do not really represent two distinct physical behaviours. Rather, they arise because most data-points in these stages correspond to a generally low WIL values, thereby forming a dense cloud near the origin (indicating that the model predicts the true response well in this region), while only a small fraction of data-points exhibit higher WIL values, which then appear as a separate, sparse cluster where the model prediction becomes poorer. It can also be noted that very few points lie close to the $x = y$ line for these three stages. This is expected, as surrogate models typically avoid making extreme predictions when extrapolating beyond the trained domain and tend to predict more a conservative value meaning that they predict values that remain closer to the bulk

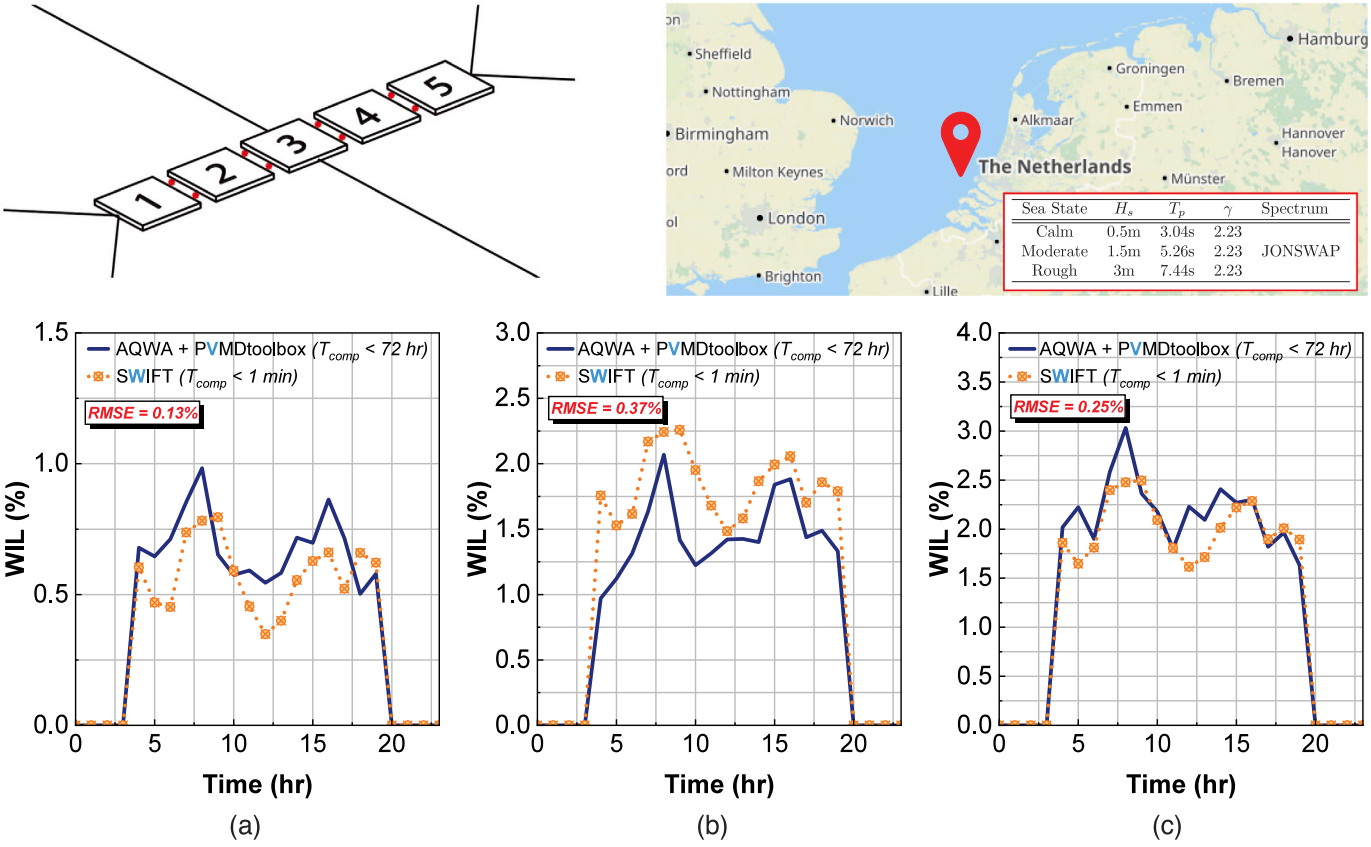

Fig. 13. Validation of SWIFT 1.0 using an independent test case consisting of 5 RP-type floaters in the North Sea, simulated under three different sea states — calm, moderate, and rough — using the theoretical JONSWAP spectrum with a wave heading of 22.5°. (a) Comparison of real-time SWIFT 1.0 predictions with the physics-based model for a calm sea state, (b) comparison for a moderate sea state, and (c) comparison for a rough sea state simulated on the 1st of June.

of the training data. Despite these effects, the overall RMSE values across all the stages remain within acceptable limits (less than 5%), as shown in Fig. 12(a), demonstrating that the model maintains a strong interpolation and extrapolation performance even under challenging conditions.

Therefore, based on this extensive evaluation, the boosted ensemble model is identified as the most robust and generalisable surrogate model for predicting WIL across varying geometrical and environmental conditions. As a practical outcome of this work in addition to answering RQ3, this model has been packaged into a MATLAB-based application - **Solar Wave-Induced Loss Forecasting Toolbox (SWIFT 1.0)** (see Section S10 of the supporting information for the user interface) as shown in Fig. 10. SWIFT 1.0 enables rapid prediction of WIL for new floating PV configurations under different operating conditions without the need for time-consuming hydro–opto–electrical simulations. It represents a physically grounded, data-driven extension of the modelling framework developed in this study. The key strengths of SWIFT 1.0 can be summarised as follows: (1) it is trained on over 50,000 WIL data points, enabling it to capture nonlinear dependencies effectively; (2) it has been thoroughly validated through a structured 13-stage testing sequence; (3) it exhibits strong interpolation and extrapolation capability; (4) it maintains an average absolute RMSE of 1%–5% relative to the physics-based model; and (5) it significantly reduces computational cost, providing accurate WIL predictions within minutes while maintaining physical interpretability.

5.3. Validation of the model

Now that SWIFT 1.0 has been developed and validated internally through the stage testing, its performance is further evaluated using an independent test case as shown in Fig. 13,Fig. 10 (via the workflow marked in orange). This case was intentionally excluded from the training dataset, making it ideal for an unbiased assessment. The selected case represents a mixed scenario in which SWIFT 1.0 is tested for both interpolation and extrapolation capabilities. Several parameters—such as unit archetype geometry, connector properties, and irradiance profile fall within the trained domain range (although not with the exact values as in the training samples), while others—including the height of the system above the water (H_{wat}), connector stiffness to damping ratio ($R_{(x/y/z)}/C_{(x,y,z)}$), mooring stiffness (k_{moor}), length of the mooring lines (L_{moor}), wave steepness (H_s/L_p), and spectral shape factor (Q_p) lie outside it. This configuration enables simultaneous testing of both interpolation and extrapolation performance under realistic conditions. Fig. 13(a–c) compares the hourly WIL predicted by the PVMDtoolbox (hydro–opto–electrical) simulations with those obtained from SWIFT 1.0 for three representative sea states—calm, moderate, and rough. Some key observations can be drawn:

(1) **Trend capture and numerical deviation:** Across all sea states, SWIFT 1.0 successfully reproduces the temporal variation of WIL, capturing the key peaks and troughs with good agreement. The close alignment of these features indicates that the model effectively captures both the amplitude and phase of the WIL response, reflecting a strong physical understanding of the underlying dynamics. Slightly larger deviations are observed under moderate-sea conditions (see Fig. 13(b)), which could be attributed to extrapolation of the particular sea state beyond the trained parameter range. Despite this, SWIFT 1.0 generalises the overall behaviour well, with RMSE values across all three sea states remaining within 0.4%. While this RMSE is already small, it becomes even more reassuring considering that many true WIL values are inherently low as seen in Fig. 13(a). This means that, for instance, considering the calm-sea WIL profile as an example,

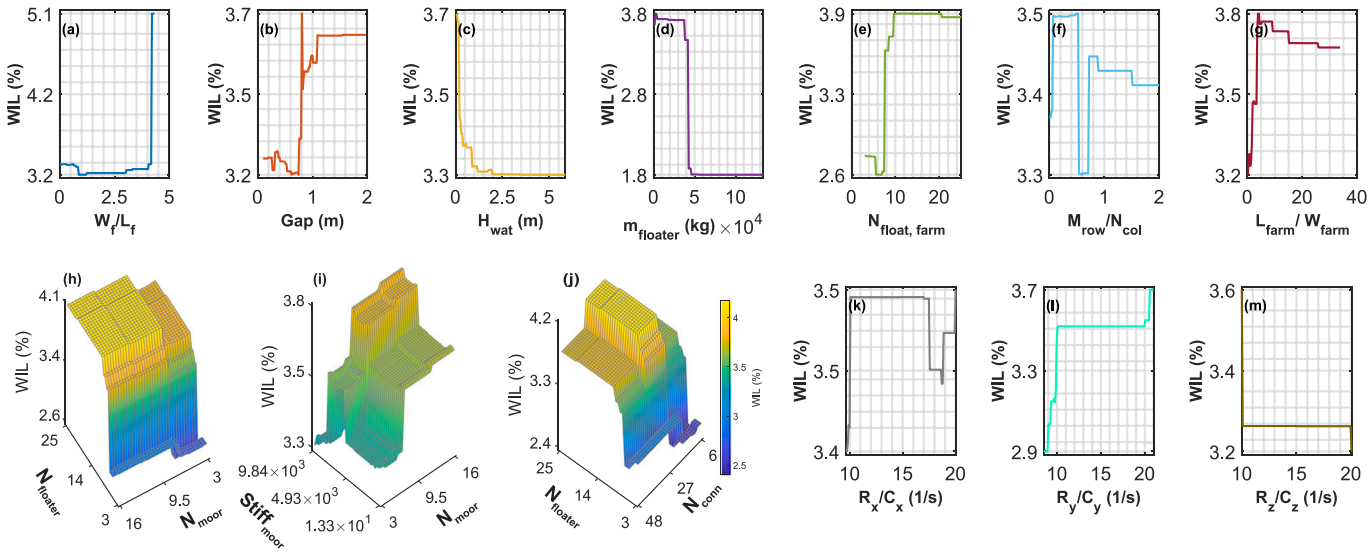

Fig. 14. Partial dependency plot of all the predictors from the hourly surrogate model. Each plots depicts the variation of WIL as a function of one predictor used in the surrogate model.

the model does not treat these low-amplitude variations as noise but successfully reproduces the true physical trends across all operating regimes, confirming its strong generalisation capability.

(2) **Computational efficiency:** In terms of computational cost, SWIFT 1.0 provides a clear advantage. The total runtime per sea-state simulation is reduced from approximately 24–72 h in the physics-based workflow (to get a one-day WIL profile) to under one minute using SWIFT 1.0, with minimal loss in predictive accuracy. This makes it a practical, ready-to-use tool capable of delivering accurate WIL forecasts with significantly reduced computational effort.

Overall, this independent validation confirms that SWIFT 1.0 accurately reproduces both the magnitude and temporal characteristics of WIL across a broad range of sea states and operating regimes. The results demonstrate its robustness, generalisation capability, and suitability as a fast and reliable WIL prediction tool for OFPV applications thereby answering the third research question **RQ3**.

6. WIL mitigation strategies and practical guidelines

Now that we have a well-validated tool to predict WIL, the next step is to evaluate its dependency on different parameters and derive a set of practical recommendations to minimise it thereby addressing the last research question **RQ4.** on *How to derive actionable, configuration-based design recommendations to minimise WIL in OFPV systems?* Since the sensitivity analysis was designed using the LHS method, understanding the full interdependency between different parameters and WIL is quite challenging. Therefore, we extract insights using the concept of partial dependency via the partial dependency plots[5] (PDPs), as shown in Fig. 14. From these plots, clear trends and directional dependencies between individual parameters and WIL can be identified, enabling us to formulate meaningful and generalisable design recommendations.

As known, the WIL depends on both geometrical and environmental parameters. However, since environmental factors such as wave and solar properties are naturally governed and cannot be physically controlled or optimised, the focus here is placed on the controllable design-based parameters. Accordingly, the PDPs shown in Fig. 14 correspond only to parameters that can be actively adjusted or optimised during the design process, enabling the derivation of simple yet practical guidelines to minimise WIL and to understand the overall direction of dependency. These PDPs are grouped into four categories based on the type of design parameter which are as follows: (1) Unit-archetype design parameters: W_f/L_f, Gap, H_{wat}, $m_{floater}$, (2) Farm-level design parameters: $N_{float,\,farm}$, M_{row}/N_{col}, L_{farm}/W_{farm}, (3) Mooring-line properties: N_{moor}, k_{moor}, (4) Interconnection properties: N_{conn}, R_x/C_x, R_y/C_y, R_z/C_z. The following recommendations can be extracted with respect to each design category.

1. Unit-archetype design recommendations

- W_f/L_f: WIL remains low and relatively stable for small to moderate aspect ratios but increases sharply at higher ratios, i.e., when $W_f/L_f \gtrsim 3$ (see Fig. 14(a)). This suggests that highly elongated or asymmetric geometries are not ideal, as they tend to amplify WIL. Therefore, a near-symmetric configuration with $W_f/L_f \approx 1$ is recommended, as it corresponds to the lowest WIL.
- *Gap*: From Fig. 14(b), a clear trend for WIL with respect to the inter-floater gap is not immediately obvious. However, it can be noted that WIL increases sharply when the gap is between 0.8 and 0.85 m. Beyond this range, WIL gradually decreases as the gap widens. This behaviour likely occurs because, at specific narrow gaps, waves can become trapped and amplified between floaters. This creates complex diffraction patterns that destabilise the modules. As the gaps widen, these interactions diminish, and the floaters begin to act more independently. Therefore, the PDP suggests maintaining a spacing of either <0.7 m or >0.85 m to keep WIL low.
- H_{wat}: WIL decreases as the vertical separation between the PV modules and the water surface increases (see Fig. 14(c)). This trend explains why elevated systems (e.g., LEP) generally exhibit lower WIL. However, this does not imply that near-surface archetypes (RP or LRP) are inherently penalised: RP/LRP designs with small drafts relative to their total thickness can still maintain low WIL. The PDP indicates that the dominant reduction in WIL occurs within the first few metres of elevation above the water; beyond approximately $H_{wat} \approx 2.5$ m, the benefit is marginal.
- $m_{floater}$: From Fig. 14(d), it can be seen that WIL decreases with increasing floater mass up to a certain point, beyond which the reduction effect saturates. This indicates that increasing floater mass beyond a threshold provides limited additional benefit while adding cost and structural complexity. Therefore, having moderately heavy floaters is advantageous. The floater mass can be adequately increased by placing multiple PV modules on a single floater, which can also help reduce the overall system cost by

lowering the total number of floaters required to meet the capacity target. However, this benefit must be balanced against the associated cost and design trade-offs.

2. **Farm-level design recommendations**

- $N_{float,;farm}$: From Fig. 14(e), it can be seen that WIL generally increases as the number of floaters increases and then begins to stabilise once the farm size exceeds approximately **10** floaters (based on the training range). This suggests that excessively long floater arrays should be avoided, as they tend to amplify the WIL. Keeping the number of floaters per row or column within a moderate range (ideally less than 8, although this may not always be practical) helps maintain lower WIL levels.
- M_{row}/N_{col}: From Fig. 14(f), it can be seen that WIL generally decreases and reaches a minimum (saddle point) when the farm layout approaches a near symmetric configuration, after which it increases slightly as the layout becomes more unbalanced. This clearly indicates that balanced or symmetric farm arrangements, where ($M_{row}/N_{col} \approx 0.8 - 1$) are preferred. Symmetric layouts ensure that the restoring forces from the mooring lines and connectors are distributed evenly, preventing localised "hotspots" of high WIL. In contrast, an unbalanced farm (very long but narrow) is more susceptible to "snaking" motions potentially increasing the WIL.
- L_{farm}/W_{farm}: From Fig. 14(g), it can be noted that the WIL increases sharply up to the point where $L_{farm} = 4 \cdot W_{farm}$, and then decreases only slightly as the farm length becomes larger than the width. This trend is primarily due to the fact that most farm arrangements in the training dataset were rectangular in nature. Therefore, if the farm is arranged like a grid/array, then it is recommended that the farm length and width are similar (symmetric with $L_{farm} \cong W_{farm}$). However, if the farm is arranged more like a string, then the farm length could be anywhere around 0.5–1.5 times the farm width to keep the WIL at a minimum.

3. **Mooring-line design recommendations**

- N_{moor}: Fig. 14(h) shows the variation of WIL with respect to N_{moor} and $N_{floaters,\ farm}$. From the plot, it can be observed that WIL increases when both the number of floaters and the number of mooring lines are high, and decreases when the number of mooring lines is high relative to a small number of floaters. This behaviour can be intuitively consistent because when there are many floaters, the interconnections already provide damping and the system should not be over-constrained with excessive mooring lines which make the response numerically unstable; whereas when there are very few floaters (low water coverage), the wave forcing could potentially dominate and more mooring lines are needed to maintain stability. The PDP therefore suggests that the mooring system should not simply be maximised/minimised but optimised. Having too few lines for few floaters can lead to dynamic instability, while too many lines for too many floaters could add cost and can even disrupt the dynamic balance without producing meaningful WIL reduction. Thus, the mooring density should be selected based on a balanced trade-off between WIL reduction, system stability, and cost.
- $Stiff_{moor}$ or k_{moor}: From Fig. 14(j), the PDP suggests that the stiffness and number of mooring lines should be co-optimised rather than varied independently, as the observed trend appears quite arbitrary. However, some general observations can still be drawn for the tested configuration which are follows: (a) The lowest WIL values are observed within the region of moderate stiffness (approximately 2–5 N/m) combined with 5–10 mooring lines, (b) It can also be noted that when the number of mooring lines increases, softer (less stiff) moorings are preferable, whereas configurations with fewer lines benefit from higher stiffness or tighter moorings. Therefore, the optimal strategy is to balance mooring stiffness, line count, and system cost—providing sufficient restraint to maintain stability without introducing unnecessary rigidity.

4. **Interconnection design recommendations**

- N_{conn}: To understand the influence of number of connectors, it has been evaluated as a function of $N_{floater}$ as shown in Fig. 14(j). From this plot, a general observation is that the connector density should scale with farm size. Within the training data, the WIL is minimal when approximately 30–40 connectors are used for farms with about 20–25 floaters, corresponding to roughly 2 connectors per floater. Below this ratio, the system becomes dynamically fragmented, while above it, further benefit is marginal. Hence, connectors should be distributed to maintain collective motion coherence without introducing excessive rigidity to keep WIL at a minimum.
- R_x/C_x, R_y/C_y, R_z/C_z: From Fig. 14(l–n), it can first be observed that the rotational stiffness-to-damping ratio about the y-axis has the most significant influence on WIL compared to the x- and z-axes. The PDPs also show that damping fractions ($> 10\% \cdot R_y$) lead to lower WIL values, whereas damping levels ($< 10\% \cdot R_y$) effectively increases the WIL. Therefore, connectors should be designed with sufficient compliance and minimal overdamping in the pitch direction to maintain synchronised motion under waves to keep the WIL at a minimum.

Therefore, based on the above PDPs, the non-linear dependency of WIL on the design parameters can be more clearly quantified, adding to the answer for RQ2 on how to quantify the WIL. The recommendations derived from these plots also provide a simple yet practical set of design guidelines to minimise WIL in OFPV systems, thereby addressing the final research question **RQ4**.

7. Limitations and scope for future work

This work establishes a robust foundation for quantifying WIL through both a physics-based framework and the SWIFT 1.0 surrogate model. However there are few limitations which also provides the scope for future work which are as follows: (i) Currently, both the physics-based and surrogate models treat the floaters and the PV modules as rigid bodies. Future research could focus on incorporating hydroelasticity to accommodate flexible platform designs and thin-film PV modules for OFPV applications. (ii) In the sensitivity analysis, we used linear mooring lines and determined the connector stiffness parameters using a scaling-based approach derived from reference studies. Future work could focus on incorporating nonlinear mooring behaviour and experimentally validated connector properties to further improve the predictive accuracy of SWIFT 1.0 for a broader range of real-world configurations. (iii) In the development of SWIFT 1.0, temperature and shading effects were not considered to solely quantify the effect of motion. Therefore, future versions of the tool could be updated to integrate other aspects affecting the EY in OFPV systems—such as shading, cooling, and soiling effects—thereby transitioning SWIFT into a comprehensive tool for energy-yield predictions. (iv) As WIL is only one component of the broader aspects affecting OFPV performance, a full economic assessment was deferred in this study. A future study, using an updated version of SWIFT, can be used to perform a more informed analysis of the economic viability of different systems across global offshore locations. (v) Although the present models are validated against multiple experimental and numerical benchmark sources available in open literature, the reliability of the current model can be strengthened further through comparisons using in-situ field measurements in the future. At present, such field measured datasets recording sea state,

platform motion, irradiance, and string-level electrical response are scarce and not yet widely available to the research community.

8. Conclusion

At the beginning of this work, we set out to answer four research questions related to modelling, quantifying, predicting, and minimising WIL for OFPV applications. The key findings with respect to each question are summarised below.

RQ1. How to develop a physics-based integrated modelling framework that accurately couples 3-D wave-structure hydrodynamics with opto-electrical performance?

- This work first presented a complete methodology for simulating the hydrodynamic response of four different archetypes using *ANSYS AQWA*, together with validation for each archetype against both experimental and computational reference studies. The average RMSE values from the validation ranged between 0.13–4 deg/m for pitch, 0.02–0.25 m/m for surge, and 0.01–0.2 m/m for heave encompassing the result across all the archetype validations.
- The validation further showed that potential-flow solvers are sufficiently accurate for EY modelling of OFPV systems, and that computationally intensive CFD tools are not strictly necessary for the purpose of "EY" estimation.
- An orientation-modelling method was introduced to convert the 3 rotational degrees of freedom from the hydrodynamic simulations into θ_t, A_z, and the extension of the *PVMDtoolbox* was described to simulate the opto-electrical analysis of OFPV systems to thereby calculate the WIL making it one of the few tools capable of simulating the EY of OFPV systems including the effect of wave motion.
- A method was proposed to estimate the long-term system response using a statistically-corrected approach that relies only on 10 min of *AQWA* simulations. This method resulted in an overall RMSE of 0.1–0.2% when compared against the reference *AQWA*-based WIL estimation.

RQ2. How to comprehensively quantify WIL through a multi-parameter (geometrical + environmental) sensitivity analysis across diverse OFPV archetypes?

- An extensive sensitivity analysis was carried out by varying 32 parameters (both design-based and environmental-based), resulting in a total of 109 simulations with over 50,000 WIL data values. The results of the sensitivity analysis showed that the RP archetype exhibits an hourly average WIL between 3%–6%, the LRP between 2.2–5.5%, and the LEP between 1.5%–4%, indicating that the LEP archetype generally yields the lowest average hourly WIL.
- The 25th–75th percentile bands also showed an overlap region across the three archetypes, indicating that each archetype can technically outperform the others under a certain combination of operating conditions.
- The sensitivity analysis further confirmed that WIL exhibits a non-linear response behaviour, with a non-linear dependency on both design-based and environmental based parameters.

RQ3. How to formulate a computationally efficient, data-driven surrogate model to predict long-term WIL for different designs and operating conditions?.

- A data-driven surrogate modelling approach was used to interpret the non-linear WIL behaviour. Several surrogate models were tested through a 13-stage validation procedure that examined both the interpolation and extrapolation capability. From this, the boosted ensemble method was selected as the best model, showing an average absolute RMSE of about 3% relative to the true WIL values.
- This model was then further used to develop a first-of-its-kind Solar Wave-Induced Loss Forecasting Tool - SWIFT 1.0 which can predict/forecast WIL for a wide range of designs and operating conditions.
- SWIFT 1.0 was trained on over 50,000 WIL data points spanning 32 varying design and environmental parameters, and further validated using an independent test case, showing an overall RMSE in the range of 0.1–0.4%. In addition, the computational time required when using SWIFT 1.0 is orders of magnitude lower compared to the full physics-based modelling framework, making it both accurate and computationally efficient.

RQ4. How to derive actionable, configuration-based design recommendations to minimise WIL in OFPV systems?

- The partial dependence of WIL on different design-based parameters was established, and a set of recommendations at the unit–archetype, farm layout, connector, and mooring-line levels were provided to help maintain WIL at a minimum.

In summary, this work delivers a complete framework that models, quantifies, predicts, and provides design guidance to reduce WIL in OFPV systems thereby addressing the key limitations in existing literature and enabling more reliable, design-informed deployment of offshore floating PV.

Notes

[1] It is important to note that the simulated results matched well with the reference data when the frequency was interpreted in Hz and the RAOs were expressed in deg/m or m/m. However, the reference article reported the units as rad/s for frequency and rad/m for the pitch RAO, which could likely be a typographical error.

[2] An SM can be interpreted as a 360° view from the PV module's perspective, indicating how the module perceives its surroundings.

[3] A skymap is a directional irradiance field that represents the sun's position and the corresponding irradiance intensity at each time step.

[4] The Fuentes thermal model is used by the toolbox to estimate $T_{mod,t}$. The model does not currently account for the effects of water temperature, and incorporating this is beyond the scope of the present work. Therefore, a constant module temperature of 25 °C is assumed throughout this study in order to isolate and quantify solely the effect of wave-induced motion on EY.

[5] A PDP illustrates how the WIL varies with respect to one parameter while keeping all other parameters fixed at their average values.

CRediT authorship contribution statement

Sathya Shanka Vasuki: Writing – original draft, Visualization, Validation, Software, Methodology, Investigation, Formal analysis, Data curation, Conceptualization. **Jack Levell:** Writing – review & editing, Visualization, Supervision, Project administration, Methodology, Funding acquisition. **Teddy Simanjuntak:** Writing – review & editing, Visualization, Supervision, Project administration, Methodology, Funding acquisition. **Rudi Santbergen:** Writing – review & editing, Visualization, Supervision, Software, Resources, Project administration, Methodology, Funding acquisition. **Olindo Isabella:** Writing – review & editing, Visualization, Supervision, Resources, Project administration, Methodology, Funding acquisition, Conceptualization.

Declaration of generative AI and AI-assisted technologies in the manuscript preparation process

During the preparation of this work, the author used ChatGPT to improve the grammar and language of few sentences to enhance readability. After using this tool/service, the author reviewed and edited the content as needed and take full responsibility for the content of the published article.

Declaration of competing interest

The authors declare that they have no known competing financial interests or personal relationships that could have appeared to influence the work reported in this paper.

Acknowledgements

The authors gratefully acknowledge Shell for their funding and valuable review of this work, while noting that the research was conducted with full independence. We also thank Youri Blom from the Photovoltaics materials and devices group at TU Delft for the discussions and help provided on expanding the PVMDtoolbox.

Appendix A. Supplementary data

Supplementary material related to this article can be found online at https://doi.org/10.1016/j.ecmx.2026.101723.

Data availability

Data will be made available on request.

References

[1] International Energy Agency (IEA). Renewables 2024: Analysis and forecast to 2030. 2024, https://www.iea.org/. [Accessed 03 April 2025].
[2] International Panel on Climate Change (IPCC). Climate Change 2023: Synthesis Report. Contribution of Working Groups I, II and III to the Sixth Assessment Report of the Intergovernmental Panel on Climate Change. 2023, https://www.ipcc.ch/. [Accessed 03 April 2025].
[3] International Renewable Energy Agency (IRENA). Tripling Renewable Power by 2030: The Role of the G7 in Turning Targets into Action. 2024, https://www.irena.org/. [Accessed 03 April 2025].
[4] International Renewable Energy Agency (IRENA), Global Renewables Alliance (GRA). Tripling renewable power and doubling energy efficiency by 2030: Crucial steps towards 1.5°C. 2023, https://www.irena.org/. [Accessed 03 April 2025].
[5] International Energy Agency. Net Zero Roadmap: A Global Pathway to Keep the 1.5 °C Goal in Reach. Paris: IEA; 2023, [Accessed 03 March 2024].
[6] Shanka Vasuki S, Levell J, Santbergen R, Isabella O. A technical review on the energy yield estimation of offshore floating photovoltaic systems. Renew Sustain Energy Rev 2025;216:115596. http://dx.doi.org/10.1016/j.rser.2025.115596.
[7] Mukhopadhyay S. Solar energy and gasification of MSW: Two promising green energy options. In: Singh VK, Bangari N, Tiwari R, Dubey V, Bhoi AK, Babu TS, editors. Green energy systems. Academic Press; 2023, p. 93–125. http://dx.doi.org/10.1016/B978-0-323-95108-1.00003-3.
[8] SolarPower Europe. Floating PV: Best Practice Guidelines. 2023, https://www.solarpowereurope.org/. [Accessed 03 March 2024].
[9] DNV. The Future of Floating Solar: Drivers and Barriers to Growth. 2022, https://www.dnv.com/. [Accessed 03 April 2025].
[10] TNO. Floating Solar Panels: Harnessing Solar Power on Water. 2024, https://www.tno.nl/en/. [Accessed 03 March 2024].
[11] POM West-Vlaanderen, Ocean Energy Europe, Parkwind, Lappeenrannan-Lahden Teknillinen Yliopisto LUT, INNOSEA, RWE Renewables GmbH, EnBW, TenneT, Exceedence Ltd, Simply Blue Group, Enel Green Power SPA, RINA Consulting SPA, Dutch Marine Energy Centre, Oceans of Energy, TU Delft, SBM Schiedam BV, Labelec, INESC TEC, WavEC, CorPower Ocean AB, Uppsala University. EU-SCORES: European Scalable Offshore Renewable Energy Source. 2023, https://euscores.eu/. [Accessed 03 March 2024].
[12] RWE. Offshore Solar: Innovative Solar Energy Projects. 2024, https://www.rwe.com/en/, [Accessed 03 March 2024].
[13] Selj J, Wieland S, Tsanakas I, Jahn U, Maugeri G. Floating Photovoltaic Power Plants: A Review of Energy Yield, Reliability, and Maintenance. IEA PVPS Task 13 (Report No. T13-31:2025), 2025, http://dx.doi.org/10.69766/KDYA8846.
[14] Maarten D, Daan van der W, Kostas S, Minne M. de J, Folkerts W. Influence of Wave Induced Movements on the Performance of Floating PV Systems. Eur Photovolt Sol Energy Conf Exhib (EU PVSEC) 2019;6DO.9.1:1759–62. http://dx.doi.org/10.4229/EUPVSEC20192019-6DO.9.1.
[15] Golroodbari SZ, van Sark W. Simulation of performance differences between offshore and land-based photovoltaic systems. Prog Photovolt. Res Appl 2020;28(9):873–86. http://dx.doi.org/10.1002/pip.3276.
[16] Bugeja R, Mule' Stagno L, Branche N. The Effect of Wave Response Motion on the Insolation on Offshore Photovoltaic Installations. Sol Energy Adv 2021;1:100008. http://dx.doi.org/10.1016/j.seja.2021.100008.
[17] Ravichandran N, Andreotti A, Pagano M, Di Pasquale A, Volpe F. Interconnection Topologies for Floating Photovoltaic System to Enhance the Power Output by Reducing the Mismatch Losses. In: 2022 IEEE PES 14th Asia-Pacific power and energy engineering conference. APPEEC, 2022, p. 1–6. http://dx.doi.org/10.1109/APPEEC53445.2022.10072079.
[18] Chen K, Li D, Wang W, Fu Q, Zhang J, Xu Y, Meng X. Wave Induced Losses Simulation of Floating Solar Photovoltaic Systems at Open Waters. In: International ocean and polar engineering conference, vol. All Days, 2023, p. ISOPE—-23–097.
[19] Bi C, Law AW-K. Co-locating offshore wind and floating solar farms – effect of high wind and wave conditions on solar power performance. Energy 2023;266:126437. http://dx.doi.org/10.1016/j.energy.2022.126437.
[20] Wang C, Song X, Fu Q, Cui L, Chen P. Design and Optimization of PV Power Supply System for Marine Buoys. J Mar Sci Eng 2023;11:1808. http://dx.doi.org/10.3390/jmse11091808.
[21] Magkouris A, Rusu E, Rusu L, Belibassakis K. Floating Solar Systems with Application to Nearshore Sites in the Greek Sea Region. J Mar Sci Eng 2023;11:722. http://dx.doi.org/10.3390/jmse11040722.
[22] Alcañiz A, Monaco N, Isabella O, Ziar H. Offshore Floating PV–DC and AC Yield Analysis Considering Wave Effects. Energy Convers Manage 2024;300:117897. http://dx.doi.org/10.1016/j.enconman.2023.117897.
[23] Alcañiz A, Agarwal S, Tiwald P, Isabella O, Ziar H, Colomés O. Assessment of power losses and structural response of offshore floating solar platform. 2025, http://dx.doi.org/10.1016/j.energy.2025.137656.
[24] Huang L, Yang Y, Khojasteh D, Ou B, Luo Z. Floating solar power loss due to motions induced by ocean waves: An experimental study. Ocean Eng 2024;312:118988. http://dx.doi.org/10.1016/j.oceaneng.2024.118988.
[25] Nysted VS, Stieng LES, Kumar M, Roosloot N, Otnes G, Kjeldstad T, Selj J. Modelling wave-induced losses for floating photovoltaics: Impact of design parameters and environmental conditions. Sol Energy 2025;293:113439. http://dx.doi.org/10.1016/j.solener.2025.113439.
[26] Luo W, Zhang X, Luo L, Tian X, Li X. Power performance of an offshore floating photovoltaic undergoing motions: Effects of dynamic incidence angle and partial shelter. Energy Convers Manage 2025;343:120215. http://dx.doi.org/10.1016/j.enconman.2025.120215.
[27] Li P, Fan L, Wang Q, Han X, Deng Z, Ren X, Zhang C, Wang J, Wang L, Huang Y. Study on hydrodynamic characteristics and power generation performance of gable-type floating photovoltaic. Energy 2025;335:138002. http://dx.doi.org/10.1016/j.energy.2025.138002.
[28] Jia G, Zhang Z, Zhao Y, Ma C, Ge X, Shu J. Effects of flexible connectors on hydrodynamic and energy output characteristics of floating photovoltaic (FPV) arrays in harsh marine environments: a physical model analysis. Renew Energy 2026;256:124266. http://dx.doi.org/10.1016/j.renene.2025.124266.
[29] Polychronakis K, Korres D, Sammoutos C, Vidalis E, Tzivanidis C. Frequency domain model of wave-induced mismatch in a moored floating solar platform with thermal effects. Sol Energy 2026;304:114180. http://dx.doi.org/10.1016/j.solener.2025.114180.
[30] Ren X, Han X, Fang Q, Li P, Zhang P, Yang W, Guo P, Wang K, Huang Y. Hydrodynamic characteristics and power generation performance of flexible floating photovoltaics. Renew Energy 2026;256:124293. http://dx.doi.org/10.1016/j.renene.2025.124293.
[31] Yang D, Shi W, Aliseda J, Gerval N, Rathakrishnan S, Ibrahim K, Lyu X, Mi C, Huang L. Digital twins for a floating photovoltaic system with experimental data mining and artificial intelligence modelling. Sol Energy 2026;305:114249. http://dx.doi.org/10.1016/j.solener.2025.114249.
[32] Inc. A. Aqwa Theory Manual. 2024, Release 2024 R1. https://www.ansys.com/.
[33] van der Zanden J, Bunnik T, Cortés A, Delhaye V, Kegelart G, Pehlke T, Panjwani B. Wave Basin Tests of a Multi-Body Floating PV System Sheltered by a Floating Breakwater. Energies 2024;17(9). http://dx.doi.org/10.3390/en17092059.
[34] van der Zanden J. Wave basin tests of multi-body floating photovoltaics system and an external floating breakwater (SUREWAVE project). 2024, http://dx.doi.org/10.5281/zenodo.10960432, Zenodo.
[35] Jiang C, el Moctar O, Schellin TE. Capability of a potential-flow solver to analyze articulated multibody offshore modules. Ocean Eng 2022;266:112754. http://dx.doi.org/10.1016/j.oceaneng.2022.112754.
[36] Jiang C, el Moctar O, Schellin TE. Hydrodynamic sensitivity of Moored and articulated multibody offshore structures in waves. J Mar Sci Eng 2021;9. http://dx.doi.org/10.3390/jmse9091028.
[37] Song J, Imani H, Yue J, Yang S. Hydrodynamic characteristics of floating photovoltaic systems under ocean loads. J Mar Sci Eng 2023;11(9). http://dx.doi.org/10.3390/jmse11091813.
[38] Yago K, Endo H. On the Hydroelastic Response of Box-Shaped Floating Structure with Shallow Draft. J Soc Nav Archit Jpn 1996;1996(180):341–52. http://dx.doi.org/10.2534/jjasnaoe1968.1996.180_341.
[39] Huang H, jun Chen X, yi Liu J, Ji S. A Method to Predict Hydroelastic Responses of VLFS under Waves and Moving Loads. Ocean Eng 2022;247:110399. http://dx.doi.org/10.1016/j.oceaneng.2021.110399.

[40] Colomés O, Verdugo F, Akkerman I. A Monolithic Finite Element Formulation for the Hydroelastic Analysis of Very Large Floating Structures. Internat J Numer Methods Engrg 2023;124(3):714–51. http://dx.doi.org/10.1002/nme.7140.

[41] Fu S, Moan T, Chen X, Cui W. Hydroelastic analysis of flexible floating interconnected structures. Ocean Eng 2007;34(11):1516–31. http://dx.doi.org/10.1016/j.oceaneng.2007.01.003.

[42] Lu D, Fu S, Zhang X, Guo F, Gao Y. A method to estimate the hydroelastic behaviour of VLFS based on multi-rigid-body dynamics and beam bending. Ships Offshore Struct 2019;14(4):354–62. http://dx.doi.org/10.1080/17445302.2016.1186332.

[43] Vogt M, Tobon CR, Alcañiz A, Procel P, Blom Y, El Din AN, Stark T, Wang Z, Goma EG, Etxebarria J, Ziar H, Zeman M, Santbergen R, Isabella O. Introducing a comprehensive physics-based modelling framework for tandem and other PV systems. Sol Energy Mater Sol Cells 2022;247:111944. http://dx.doi.org/10.1016/j.solmat.2022.111944.

[44] Santbergen R, Muthukumar V, Valckenborg R, van de Wall W, Smets A, Zeman M. Calculation of irradiance distribution on PV modules by combining sky and sensitivity maps. Sol Energy 2017;150:49–54. http://dx.doi.org/10.1016/j.solener.2017.04.036.

[45] McKay MD, Beckman RJ, Conover WJ. A comparison of three methods for selecting values of input variables in the analysis of output from a computer code. Technometrics 1979;21. http://dx.doi.org/10.2307/1268522.

[46] Dassault Systèmes SOLIDWORKS Corp. Solidworks — 3D CAD design software. 2025, URL https://www.solidworks.com/. [Accessed 03 April 2025].

[47] Hersbach H, Bell B, Berrisford P, Hirahara S, Horányi A, Muñoz-Sabater J, Nicolas J, Peubey C, Radu R, Schepers D, Simmons A, Soci C, Abdalla S, Abellan X, Balsamo G, Bechtold P, Biavati G, Bidlot J, Bonavita M, De Chiara G, Dahlgren P, Dee D, Diamantakis M, Dragani R, Flemming J, Forbes R, Fuentes M, Geer A, Haimberger L, Healy S, Hogan RJ, Hólm E, Janisková M, Keeley S, Laloyaux P, Lopez P, Lupu C, Radnoti G, de Rosnay P, Rozum I, Vamborg F, Villaume S, Thépaut J-N. Complete ERA5 from 1940: Fifth generation of ECMWF atmospheric reanalyses of the global climate. 2017, http://dx.doi.org/10.24381/cds.143582cf, Copernicus Climate Change Service (C3S) Data Store (CDS). [Accessed 01July 2025].

[48] Maritime V. The douglas sea scale – a classification of the conditions at sea. 2023, URL https://ventomaritime.dk/blog/douglas-sea-scale. [Accessed 03 April 2025].

[49] Meteotest AG. Meteonorm — Climatic data & solar radiation software. 2025, URL https://www.meteonorm.com/en/. [Accessed 03 April 2025].

[50] The MathWorks, Inc. Machine learning in MATLAB. 2025, https://nl.mathworks.com/help/stats/machine-learning-in-matlab.html. [Accessed: 01 July 2025].